Journal of Nanobiotechnology

RESEARCH

Open Access

# Intranasal delivery of small extracellular vesicles reduces the progress of amyotrophic lateral sclerosis and the overactivation of complement-coagulation cascade and NF-κB signaling in *SOD1$^{G93A}$* mice

Jinrui Zhou[1†], Fuxiang Li[2†], Bin Jia[2†], Zicong Wu[3,4], Zhonghai Huang[2], Meiting He[2], Huandi Weng[2], Kwok-Fai So[2,5,6,7,8], Wenrui Qu[1*], Qing-Ling Fu[3,4,10*] and Libing Zhou[2,5,6,7,8,9*]

## Abstract

Amyotrophic lateral sclerosis (ALS) is a fatal disease characterized by progressive motoneuron degeneration, and effective clinical treatments are lacking. In this study, we evaluated whether intranasal delivery of mesenchymal stem cell–derived small extracellular vesicles (sEVs) is a strategy for ALS therapy using *SOD1$^{G93A}$* mice. In vivo tracing showed that intranasally-delivered sEVs entered the central nervous system and were extensively taken up by spinal neurons and some microglia. *SOD1$^{G93A}$* mice that intranasally received sEV administration showed significant improvements in motor performances and survival time. After sEV administration, pathological changes, including spinal motoneuron death and synaptic denervation, axon demyelination, neuromuscular junction degeneration and electrophysiological defects, and mitochondrial vacuolization were remarkably alleviated. sEV administration attenuated the elevation of proinflammatory cytokines and glial responses. Proteomics and transcriptomics analysis revealed upregulation of the complement and coagulation cascade and NF-κB signaling pathway in *SOD1$^{G93A}$* mouse spinal cords, which was significantly inhibited by sEV administration. The changes were further confirmed by detecting C1q and NF-κB expression using Western blots. In conclusion, intranasal administration of sEVs effectively delays the progression of ALS by inhibiting neuroinflammation and overactivation of the complement and coagulation cascades and NF-κB signaling pathway and is a potential option for ALS therapy.

[†]Jinrui Zhou, Fuxiang Li and Bin Jia contributed equally to this work.

*Correspondence:
Wenrui Qu
quwenrui@jlu.edu.cn
Qing-Ling Fu
fuqingl@mail.sysu.edu.cn
Libing Zhou
tlibingzh@jnu.edu.cn

Full list of author information is available at the end of the article

**Graphical abstract**

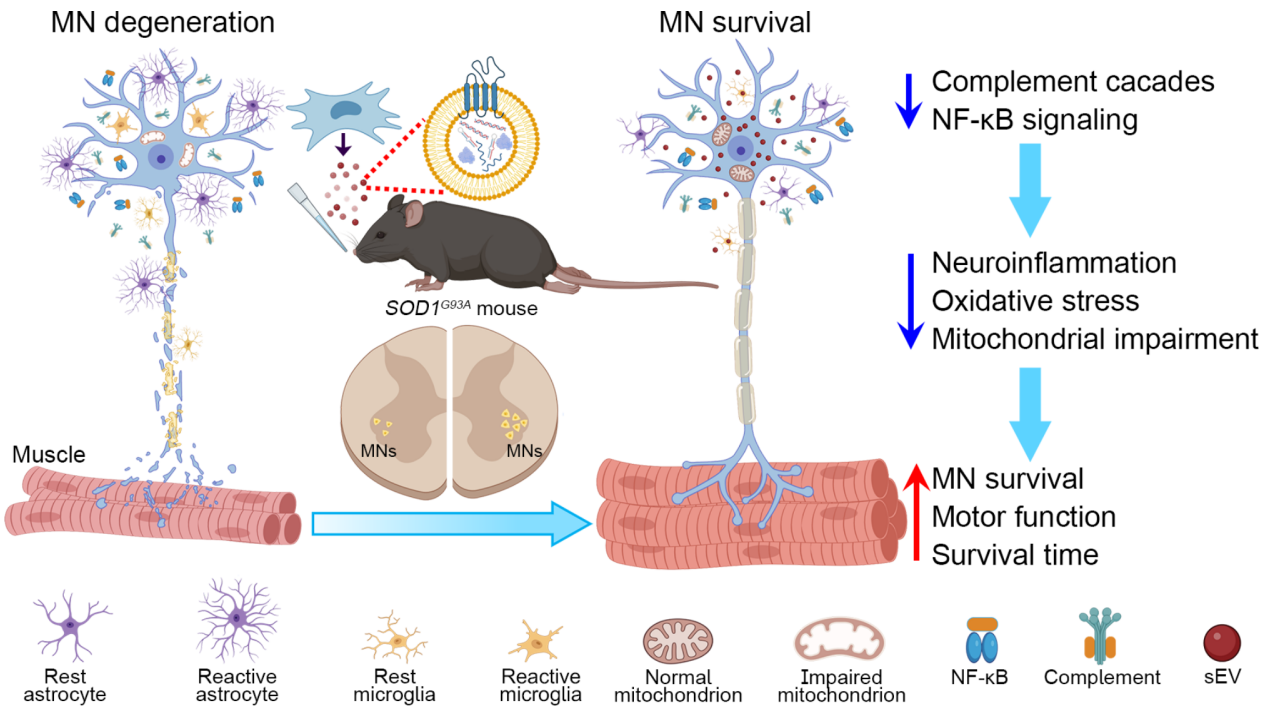


**Keywords** Small extracellular vesicles, Amyotrophic lateral sclerosis, Intranasal administration, Complement & coagulation cascade, NF-κB signaling, Motoneuron degeneration, Neuroinflammation, Transgenic mouse, Proteomics, Transcriptomics

## Introduction

Amyotrophic lateral sclerosis (ALS) is characterized by chronic progressive degeneration of motoneurons in the cerebral cortex, brainstem, and spinal cord [1]. Most patients with ALS die within 3–5 years of onset because of muscle paralysis and respiratory failure [2]. Approximately 90–95% of cases are sporadic ALS without apparent genetic linkage and 5–10% of cases are caused by genetic abnormalities (familial ALS). *SOD1*, which encodes a cytoplasmic copper/zinc superoxide dismutase, is the first identified gene associated with ALS, and mutations in *SOD1* are the primary cause of 15–20% of familial ALS cases [3]. Mutant SOD1 impairs the clearing superoxide by mitochondria and leads to oxidative damage in neurons. Other candidate and risk genes have been identified such as *TDP43*, *C9orf72*, *ANXA11*, *KIF5A* [4], and *KANK1* [5]. The symptoms of sporadic and familiar ALS are indistinguishable, although they show differences in pathology.

The potential mechanisms of ALS development are not completely understood. Motoneuron death may be caused by oxidative stress, glutamate excitotoxicity, mitochondrial dysfunction, and neuroinflammation [6]. Currently, the therapeutic strategy for ALS is to alleviate pathological processes and delay motoneuron death. Riluzole and Edaravone are the two drugs approved by FDA for ALS. As a glutamate antagonist, Riluzole is proposed to alleviate excitotoxic death of motoneurons by reducing cellular calcium influx and damage to the endoplasmic reticulum [7]. Edaravone is a reactive oxygen species (ROS) scavenger that reduces neuronal damage by inhibiting oxidative stress [8]. However, the contributions of these drugs to prolonging survival time and improving quality of life patients are limited and they also have side effects on other organs [9].

Great efforts have been made to develop novel therapeutic strategies for ALS, and stem cell–based therapies are attractive options. Stem cells exhibit multiple beneficial effects, including immunomodulation, anti-neuroinflammation, and neuroprotection activities through releasing cytokines and factors [10]. Mesenchymal stem cells (MSCs) derived from different tissues have been investigated in animal experiments [11, 12], and promising results from stem cell therapy have been reported in recent clinical trials [13–15]. In our previous studies, we established human urine epithelial cells-induced pluripotent stem cells (iPSCs), which could be further induced into MSCs (iPSC-MSCs). Our comparative studies

revealed several advantages of iPSC-MSCs over adult bone morrow-derived MSCs (BM-MSCs). First, iPSC-MSCs were insensitive to proinflammatory-induced human leukocyte antigen-II expression and showed a stronger immune privilege after transplantation compared to adult BM-MSCs [16]. Second, iPSC-MSCs maintained a better capacity of proliferation than BM-MSCs [17]. However, stem cell therapy faces many challenges for clinical application, including transplantation routes and frequency, cell survival, and immune rejection [18].

Small extracellular vesicles (sEVs) are nanoparticles with a diameter of 30–200 nm that are released by most eukaryotic cells and act as mediators for intercellular communication [19]. MSC-derived sEVs are promising alternatives for stem cell–based therapies because of several specific advantages. MSC-derived sEVs easily bypass the brain-blood barrier (BBB) to penetrate nervous tissues, contain most components of stem cells while lacking a cellular structure, show low immunogenicity, and function as drug carriers [20]. Increasing evidence has demonstrated that the beneficial effects of stem cell–based therapies is mainly attributed to sEVs released from the transplanted cells, and the miRNA and protein cargos enriched in sEVs were shown to facilitate neural repair in neurological disorders [21]. MSC-derived sEVs maintain therapeutic efficacy independent of their parent cells and can overcome the difficulties in the clinical application of cell transplantation.

Because of their small sizes, sEVs can reach the central nervous system (CNS) through various delivery routes. After intranasal delivery, sEVs readily reach the brain parenchyma directly from the nasal cavity without crossing the BBB; this administration method can be applied for many neurological disorders [22]. Moreover, in vivo neuroimaging showed that these sEVs specifically target and accumulate in pathological brain regions [23]. Our recent studies showed that intranasally administered MSC-derived sEVs robustly alleviated neuroinflammation and fostered neural repair through their cargos in a cerebral ischemia mouse model [24].

In the current work, we prepared sEVs from human urine epithelial cells-derived iPSCs-induced MSCs and evaluated the therapeutic effects of intranasally delivered sEVs for ALS using $SOD1^{G93A}$ transgenic mice, a classic ALS mouse model [25]. We studied the biodistribution of sEVs in the CNS and the effects of sEVs on motor function and survival in $SOD1^{G93A}$ mice. Typical pathological changes of ALS progression were studied in these mice, including spinal motoneuron number and synaptic innervation, myelin sheath and mitochondria morphology, neuromuscular junctions (NMJs) and their electrophysiological function, and neuroinflammation. After sEV administration, spinal samples were collected for cytokine, proteomic, and transcriptomic analysis to investigate the potential mechanisms of sEV therapeutic effects. Our results demonstrated that intranasal administration of sEVs reduced the progression of ALS (motor performance and survival time), alleviated motoneuron-related pathological changes and neuroinflammation, and inhibited the complement-coagulation cascade and nuclear factor kappa-B (NF-κB) signaling pathways. These findings indicate that intranasal administration of sEVs is a potential therapeutic strategy for ALS.

## Materials and methods

### Preparation and characterization of sEVs

MSCs were derived from iPSCs induced from human urine epithelial cells, and anion-exchange chromatography was used to prepare sEVs from MSCs [26]. Briefly, frozen MSCs were recovered and cultured in 150 $cm^2$ culture plates in complete culture medium; the cells were then passaged to the 5-stack cell factories. After cell confluence reached 80–90%, cells were washed and incubated with chemically defined and protein-free medium for 6 h. The medium was replaced with fresh protein-free medium, and cell supernatants were harvested after 42 h. After centrifugation for 20 min at 2000x g, sEVs in the supernatants were isolated by anion-exchange chromatography (Mylab, Guangzhou, China) according to the manufacturer's protocol. sEVs characteristics were evaluated by NanoSight, electron microscopy, and western blots as described [24]. In addition, we prepared mCherry-labelled sEVs for in vivo tracing studies as described before [26]. Briefly, cultured MSCs were transfected with lentivirus vectors-loaded mCherry-CD63 fusion gene under EF1A promoter (pLV [Exp]-Puro-EF1A > mCherry (ns): hCD63) and sEVs were then isolated as described above. Flow cytometry confirmed that more than 90% of sEVs were positive for mCherry.

### Animals and experimental groups

Animal studies were performed following the National Institutes of Health Guide for Care and Use of Laboratory Animals and approved by the Animal Ethics Committee of Jinan University (Approval No.: IACUC-20230831-09). Transgenic mice overexpressing human SOD1 carrying the Gly93Ala mutation ($SOD1^{G93A}$) were purchased from Jackson Laboratories (stock number 002726, USA), and wildtype (WT) mice (C57BL/6J) were obtained from Beijing Vital River Laboratory Animal Technology Co., Ltd. Animals were housed under controlled environmental conditions ((22 ± 1) °C, (55 ± 10) % humidity, 12-hour light/dark cycles). The following primers were used for genotyping: 5′-CATCAGCCCTAATC CATCTGA-3′ and reverse 5′-CGCGACTAACAATCAA AGTGA-3′. $SOD1^{G93A}$ heterozygous mice (13 weeks old) were randomly assigned to the sEV and the phosphate

buffered saline (PBS) (the same amount of PBS administration) groups. Age-matched WT mice (WT) were used as the reference. Behaviors and weight were collected at baseline before sEV or PBS administration. The basic conditions of all mutant mice (death, activity, eating, etc.) were carefully recorded every day, and the survival curve of mutant mice was drawn after excluding the mice that were sacrificed at 20 weeks for pathology and other studies.

#### In vivo tracing of sEVs

Approximately 10–15 μl of mCherry-labelled sEVs ($3.0\times10^9$ nanoparticles/delivery) were intranasally delivered to adult *SOD1*$^{G93A}$ mice daily for 2 consecutive days. Animals were perfused with 4% paraformaldehyde 24 h after the last delivery. Immunostaining was performed on frozen sections (30-μm thickness) using the following primary antibodies: goat anti-choline acetyltransferase (ChAT; 1:500, AB144p, Millipore), rabbit anti-NeuN (1:1000; ab177487; Abcam), rabbit anti-Iba1 (1:1000; 019-19741; Wako), and rat anti-glial fiber acid protein (GFAP; 1:500; 13–0300; Thermo Fisher). Sections were analyzed by confocal microscopy (Zeiss 780, Germany).

#### Behavioral tests

All animals underwent behavioral tests before and once a week after intranasal administration. Three days of pretraining were performed before the first test.

*Grip strength tests* The measurement of forelimb strength was conducted using a gripping meter (NO47200; Ugo Basile; Italy). Maximal values were taken from three trials in each mouse.

*Rotarod tests* Mice were placed on an accelerating rotarod (600; Ugo Basile; Italy), with an increase from 5 to 40 rpm. The stay duration was recorded for each mouse. The average value was calculated from three tests in each animal.

#### Electromyogram (EMG) recording

After anesthetization of mice with propofol (20 μL/g), the sciatic nerve and gastrocnemius muscle were exposed under a stereomicroscope. A recording electrode was inserted into the gastrocnemius, and a stimulation (5000 mV, 0.1 ms) was administered to the sciatic nerve using a monopolar stimulation electrode. EMG signals were collected using a multi-channel system (VikingQuest EMG/EP System, Nicolet, USA). For each animal, the recoding was repeated at least six times with an interval of 3 min, and the average result was determined.

#### Pseudorabies virus (PRV) tracing

After anesthetization of mice with isoflurane, the sciatic nerve trunk was exposed and 1 μL PRVP (109 PFU/mL, P03001, BrainVTA, China) was injected into the trunk using a 32-gauge Hamilton syringe. After 48 h, mice were perfused by 4% paraformaldehyde and lumbar spinal cords were collected. PRV-labelled neurons were analyzed in 30 μm frozen spinal sections by confocal microscopy (Zeiss 700, Germany).

#### Electron microscopy (EM)

Mice were intracardially perfused by fixative (2.5% glutaraldehyde+2% paraformaldehyde), and L2–L5 spinal segments were dissected out. Under a dissection microscope, unilateral ventral portions (including ventral horn) of spinal tissues and sciatic nerves were isolated and fixed in the same fixative at 4 °C for approximately 24 h. Samples were subjected to PBS washing, incubation with 1% osmic acid (at least 1.5 h), ethanol dehydration, and infiltration with acetone and epon 812 (1:1) for 3–4 h. Samples were then embedded using resin (EMbed 812; Electron Microscope Sciences). The blocks were cut into 60 nm sections by a Leica ultramicrotome, followed by uranyl acetate and lead citrate stain. Images were captured by a transmission electron microscope (JEM-1400 PLUS; Japan Electron Optics Laboratory Co., Ltd.). Individual large motoneurons in the ventral horn were identified and the images of mitochondria were captured in motoneurons. ImageJ was used to measure total mitochondria surface area ($\mu m^2$; outer membrane area and cristae area folded by inner membrane), mitochondrial cristae area ($\mu m^2$), perimeter (μm), aspect ratio (major axis)/(minor axis), and vacuolation ratio (area short of mitochondrial cristae/total mitochondrial area). Total mitochondria in at least six motoneurons were analyzed in each sample. The G-ratio was calculated as the ratio of the inner to the outer diameter of myelin sheath. Three animals in each group were analyzed.

#### Immunofluorescent and histological staining

Animals were perfused with 4% paraformaldehyde in 0.01 M PBS. Spinal cords and gastrocnemius were collected and sections were prepared with a sliding microtome (Leica, Germany). Floating methods were used for immunostaining. Briefly, after washing with 0.01 M PBS plus 0.3% Triton, sections were blocked in 3% bovine serum albumin plus 10% normal donkey serum for 2 h and incubated with primary antibodies overnight at 4 °C. In each spinal block, six series of alternative transverse spinal Sect. (30-μm thickness) were prepared, and one serial of sections in each animal sample were subjected to immunostaining using one type of primary antibody. Primary antibodies included goat anti-choline acetyltransferase (ChAT; 1:500; AB144p, Millipore), rabbit anti-Iba1 (1:1000; 019-19741, Wako), rabbit anti-NeuN (1:1000; ab177487, Abcam), and goat anti-synaptophysin (1:500; GT2589, Gene Tex). The sections were then incubated

with fluorescent secondary antibodies. To examine acetylcholine receptors (AchRs) in gastrocnemius muscles, one serial of frozen sections from one muscle (8 serials in total, 40-μm thickness) were stained by α-bungarotoxin conjugated to Alexa Fluor 546 (*α*-BT; 1:1,000, T1175, Molecular Probes). Sections were examined by confocal microscopy (Zeiss 700, Germany). The average number of AchRs per section was calculated per animal. Identification of fragmented AchRs was performed as described [27]. Three-dimensional AchRs were reconstructed and their surface areas were calculated using Imaris software. Liver, spleen and kidney morphology was examined in paraffin sections stained by hematoxylin and eosin (HE).

#### Proteomics analysis

We collected fresh spinal samples (ventral portions of lumbar spinal segments) and proteomic analysis of these samples was conducted by the Gene Denovo Biotechnology Co. (Guangzhou, China). Briefly, tissues were homogenized in lysis buffer (2% SDS, 7 M urea, 1 mg/mL protease inhibitor cocktail) for 3 min on ice using an ultrasonic homogenizer, and the supernatants were collected after centrifugation at 14 000 rpm for 15 min at 4 °C. The protein concentration was measured using a BCA Protein Assay Kit. The proteins were digested with sequence-grade modified trypsin (Promega, Madison, WI, USA) at a substrate/enzyme ratio of 50 : 1 (*w*/*w*) at 37 °C for 16 h. The digested proteins were subjected to high PH reverse phase separation using the Ultimate 3000 system (ThermoFisher Scientific, MA, USA) connected to a reverse phase column (Waters Corporation, MA, USA). After the fractions were collected and dried, they were subjected to nano-HPLC-MS/MS analysis using on-line nanospray LC-MS/MS on an Orbitrap Fusion Lumos coupled to an EASY-nLC 1200 system (Thermo Fisher Scientific, MA, USA). The mass spectrometer was run under data independent acquisition (DIA) mode and automatically switched between MS and MS/MS mode. Raw data of DIA were processed and analyzed by Spectronaut X (Biognosys AG, Switzerland) with default parameters. Differentially expressed proteins (DEPs) were defined as those with a *Q* value (FDR) < 0.05 and |log2foldchange| > 0.58. The protein function and classification were analyzed using Gene Ontology (GO) and Kyoto Encyclopedia of Genes and Genomes (KEGG) analyses. Gene Set Enrichment Analysis (GSEA) was performed using the GSEA software and MSigDB to identify a set of genes in specific GO terms/pathways with significant differences; enrichment scores and P value were calculated using default parameters. Three animals in each group were used.

#### RNA sequencing (RNAseq) of spinal samples

Fresh cervical spinal segments were collected for RNA-seq, which was performed by the Novogene Company (Suzhou, China). Briefly, RNA was extracted from tissues using the TRIzol Plus RNA Purification Kit (Cat. No. 12183018 A, Invitrogen Life Technologies), and mRNA was purified using poly-T-oligo-attached magnetic beads. cDNA was synthesized using reverse transcriptase, and PCR was performed with Phusion High-Fidelity DNA polymerase, universal primers, and index primer. The samples were then sequenced on an Illumina Novaseq platform and 150 bp paired-end reads were generated. Gene expression was calculated using fragments per kilobase of exon per million fragments mapped (FPKM), and differentially expressed genes (DEGs) were identified using the DESeq2 R package (1.20.0). Genes with an adjusted P-value (Padj) ≤ 0.05 in the DESeq2 were assigned as DEGs. The clusterProfiler R package was used for GO enrichment and KEGG analysis. Three animals were used in each group.

#### Cytokine analysis

After 4 weeks of intervention, spinal lumbar enlargement of $SOD1^{G93A}$ mice was collected for cytokine analysis; spinal samples of matched-age WT mice were used as the control. Samples were homogenized in lysis buffer (150 mM NaCl, 20 nM Tris-HCl, 1 mM EDTA, 1 mM EGTA, 1% Triton-X-100, pH 7.5) and cytokine levels were measured using Luminex at the Shanghai Univ Biotechnology Co., Ltd. (China). The analyzed cytokines included IL-1β, tumor necrosis factor-α (TNF-α), interferon-γ (IFN-γ), IL-2, IL-6, IL-4, IL-5, IL-10, keratinocyte chemoattractant (KC), and IL-12 (p70). Three animals in each group were analyzed.

#### Western blots

Spinal samples were collected from $SOD1^{G93A}$ mice after 4 weeks of intervention (approximately 18 weeks old) and age-matched WT mice. Protein extraction was performed using RIPA lysis buffer (Beyotime Biotechnology, Shanghai, China), and the concentration was measured by a BCA kit (Beyotime Biotechnology). Proteins were separated on 8% sodium dodecyl sulfate polyacrylamide gels and then transferred to PVDF membranes (Millipore, MA, USA). The membranes were blocked in 5% bovine serum and then incubated at 4 °C for at least 24 h with the following antibodies: rabbit anti-C1q (1:1000; ab155052, Abcam), mouse anti-NF-κB (1:1000; 6956, Cell Signaling Technology), rabbit anti-β-Tubulin (1:1000; 2128, Cell Signaling Technology), and rabbit anti-GAPDH (1:1000; 5174, Cell Signaling Technology). There were at least three biological replicates in each group. The relative expression levels were calculated by measuring grayscale values of bands using ImageJ.

### Statistical analysis

Data were presented as mean ± SEM and analyzed by GraphPad Prism 9.0.0. Behavioral tests were compared by two-way ANOVA and Bonferroni post hoc comparison, and survival curves were analyzed by Gehan-Breslow-Wilcoxon. Other comparisons were performed by one-way ANOVA multiple comparison. $P<0.05$ was considered significant.

## Results

### Preparation of high-purity sEVs from MSCs

We cultured iPSC-derived MSCs and purified sEVs from MSCs using anion exchange chromatography (Fig. 1A). NanoSight detection of sEVs revealed uniform nanoparticles in sizes, with a peak at approximately 100 nm in diameter (Fig. 1B). Transmission electronic microscopy showed that sEVs were bilipid-layered nanoparticles (Fig. 1C). Western blots of sEVs and MSCs confirmed that sEVs were positive for Alix, CD63, CD9 and TSG101 and negative for Calnexin (an endoplasmic reticulum–associated protein not found in sEVs) (Fig. 1D). These results indicate the successful generation of MSC-derived sEVs with high purity.

### Intranasally-delivered sEVs are widely distributed in the brain and spinal cord of *SOD1*$^{G93A}$ mice

Biodistribution of sEVs after intranasal administration was traced using mCherry-labelled sEVs, which were obtained from MSCs transfected with LV-CMV-mCherry-WPRE-pA during sEV preparation [24]. Fourteen-weeks old *SOD1*$^{G93A}$ mice received mCherry-sEVs through intranasal delivery daily for 2 days, and brain and spinal cord tissues were collected 24 h after the last administration. In the sagittal sections, mCherry-positive particles were visible in the olfactory bulb, cortex, red nuclei, and pons (Fig. 2A). In the transverse spinal sections, mCherry-labelled sEVs were mainly distributed in the gray matter and barely visualized in the white matter (Fig. 2B). In anti-ChAT immunostained sections, some spinal motoneurons were still preserved in the ventral horn and filled with mCherry-labelled nanoparticles in their soma, as shown in the merged images (Fig. 2B). Spinal neurons were visualized using anti-NeuN immunostaining and many mCherry-labelled nanoparticles were surrounding or in spinal interneurons (Fig. 2C). Abundant reactive astrocytes were distributed in the entire spinal cord of *SOD1*$^{G93A}$ mice and few mCherry-labelled nanoparticles were ingested by astrocytes (Fig. 2D). Anti-Iba1 immunostaining showed a strong microglial response in the spinal section of *SOD1*$^{G93A}$ mice as indicated by microglia with enlarged soma and well-identified processes; mCherry-labelled nanoparticles were found in some microglia (Fig. 2E). We also studied sEV biodistribution after intranasal administration of mCherry-labelled sEVs at day 120 and day 60 in *SOD1*$^{G93A}$ mice, which represented the later stage of ALS development and the stage before ALS onset respectively. At day 120, the biodistribution of mCherry-sEVs in vivo was similar to that after intranasal administration at 14 weeks (Fig. S1). mCherry-sEVs were also visible in the brain and spinal cord after intranasal administration at day 60 (Fig. S2), while the number of mCherry-labelled nanoparticles was less than that after intranasal administration at the later stages. These findings indicate sEVs are efficiently transported to the brain and spinal cord of *SOD1*$^{G93A}$ mice after intranasal administration and widely penetrated into neurons and some microglia, and that the penetration of sEVs into the CNS is also affected by the ASL development.

### sEV administration prolongs survival time and improves motor function in *SOD1*$^{G93A}$ mice

*SOD1*$^{G93A}$ mice are the first established ALS transgenic mouse model; these mice become paralyzed in one or more limbs because of motor neuron loss from the spinal cord and die by 5–6 months of age [25]. Abnormal behaviors are detected in mice 12–14 weeks old, indicating an early onset of pathological process. To evaluate the therapeutic effect of sEVs on the disease progression of ALS, sEVs were intranasally delivered to 14-week-old *SOD1*$^{G93A}$ mice and continued once every two days for one month; behaviors were studied prior to and after the intervention (Fig. 3A). The control (PBS) group received the same amount of PBS. The body weight of *SOD1*$^{G93A}$ mice was relatively stable after administration compared with the baseline; there was no significant difference in the two groups despite a small decrease in the sEV group at 18 weeks (Fig. 3B).

Progressive paralysis of skeletal muscles is a symptom of ALS. We measured grip strength of limbs, calculated as the ratio to baseline, and observed a rapid decrease from 14 weeks onwards in the PBS group (Fig. 3C). In contrast, the grip strength in the sEV group showed a slight increase at 15 weeks and was relative stable thereafter, with a significant increase compared with the PBS group at 18 weeks (Fig. 3C). In accelerating rotarod tests, the falling latency of the PBS group gradually decreased from 15 weeks, while it did not significantly change compared with baseline in the sEV group (Fig. 3D). At 18 weeks, the falling latency (ratio to baseline) was 0.69 ± 0.06 in the PBS group and 0.92 ± 0.09 in the sEV group, with a significant difference between the two groups (Fig. 3D).

The mice in the PBS group exhibited paralysis at 18 weeks and thus we stopped behavioral tests to avoid any interference or undue stress. In the PBS group, the first mouse died at day 133 (19 weeks), and approximately 27% (3/11) of mice were alive at day 168 (24 weeks). These

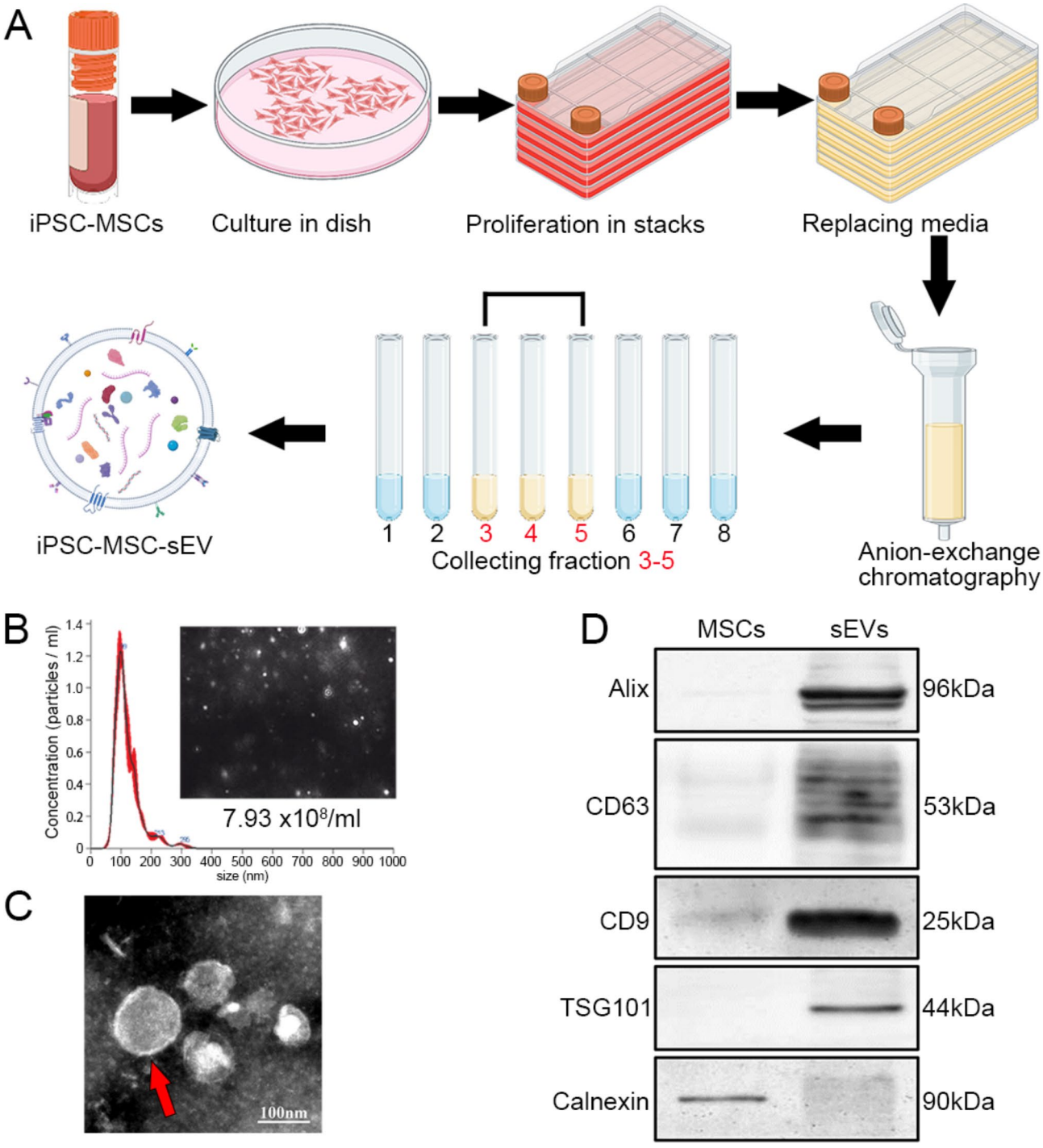


**Fig. 1** Purification and characterization of MSC-derived sEVs. **A**: Schematic of the preparation of iPSC-derived MSCs and the purification of sEVs from MSCs using anion-exchange chromatography. **B**: NanoSight of sEVs showed a sharp peak of nanoparticle concentration at about 99 nm in diameter; the average diameter was 120.8 ± 2.2 nm and the concentration was $7.93 \times 10^8$ nanoparticles / ml under the 200-times dilution. **C**: sEVs were characterized as bilayer nanoparticles (red arrow). **D**: In western blots, sEVs expressed specific markers (Alix, CD63, CD9, and TSG101) and were negative for Calnexin; MSCs were negative for sEV-specific markers but positive for Calnexin

survived mice were very weak and failed to move around freely for eating, and we defined 168 days (24 weeks ) as the endpoint of the experiment. In contrast, in the sEV group, the first mouse died at day 164 and approximately 78% (7/9) of mice were alive at day 168 (24 weeks). The survival rate was significantly increased in the sEV group compared with the PBS group (Fig. 3E). At the end of the experiment, organs (liver, spleen, and kidney) were

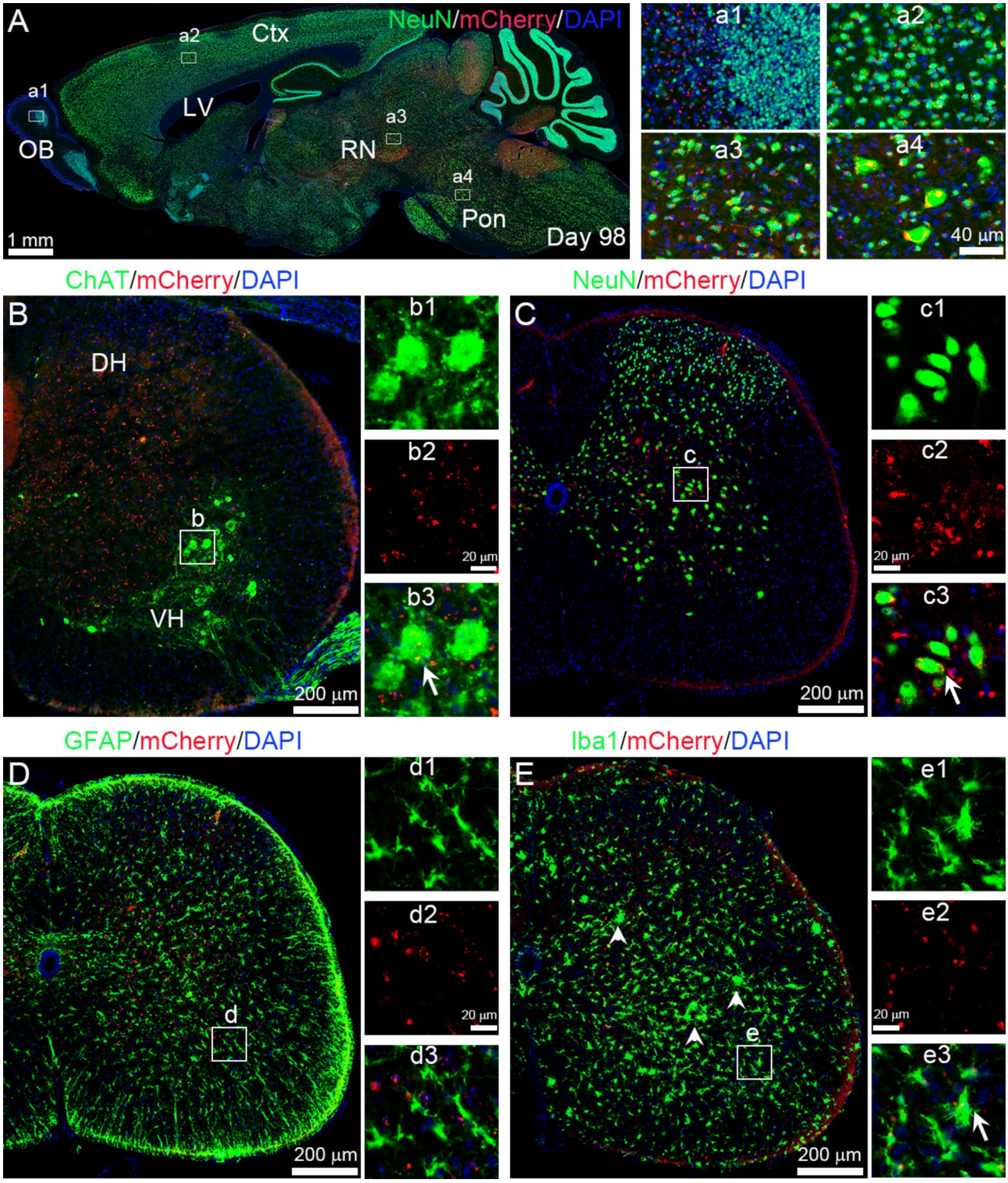


**Fig. 2** (See legend on next page.)

collected; HE stain did not show any marked differences among the three groups (Fig. S3).

### sEV administration reduces spinal motoneuron death and synaptic denervation in *SOD1*$^{G93A}$mice

Motoneuron loss and axon denervation are typical pathological features in the ALS progression. In mutant mice

(See figure on previous page.)

**Fig. 2** Biodistribution of sEVs in the brain and spinal cord of*SOD1*$^{G93A}$mice after intranasal administration. Fourteen-weeks old *SOD1*$^{G93A}$ mice were subjected to intranasal administration of mCherry-labelled sEVs daily for 2 days and mCherry-labelled nanoparticles were visualized in the brain and spinal cord sections. **A**: In the sagittal section, mCherry-labelled nanoparticles (red) were widely distributed in the olfactory bub (OB, a1), cortex (Ctx, a2), diencephalon, and brain stem such as red nuclei (RN, a3) and pontine (Pon, a4) nuclei. Neurons were immunostained by anti-NeuN antibodies (green) and nuclei were stained by DAPI (blue). **B**–**E**: Transverse lumbar spinal sections were immunostained for ChAT (**B**), NeuN (**C**), GFAP (**D**), and Iba1 (**E**). Abundant mCherry-labelled nanoparticles (red) were visible in the gray matter, but not in the white matter. In the anti-ChAT immunostained section (**B**), some spinal motoneurons (green) were preserved in the ventral horn (VH) and filled with red nanoparticles in their soma (arrow) as shown in the images with high magnification (b1–b3). Anti-NeuN immunostaining labeled all spinal neurons (green, **C**), and red nanoparticles also surround and/or penetrate spinal interneurons (arrow, c1–c3). GFAP-positive astrocytes (green) were widely distributed in the entire spinal cord (**D**), whereas few nanoparticles were found in astrocytes (d1–d3). In the anti-Iba1 immunostained section (**E**), some microglia (green) showed enlarged somas (arrows) and nanoparticles were ingested by microglia (e1–e3, arrow). DH, dorsal horn. Same scale bar in **B**–**E**

after 4 weeks of intervention and age-matched WT mice (18 weeks old), PRV was unilaterally injected into sciatic nerves and retrograded-labelled lumbar spinal motoneurons were analyzed at the ipsilateral side (Fig. 4A–C). In the WT mice, many spinal motoneurons were well traced and their dendrites were readily visualized (Fig. 4A), whereas rare motoneurons in the PBS group and some motoneurons in the sEV group were observed (Fig. 4B, C). The average numbers of PRV-labelled motoneurons per section were 9.2 ± 0.6 in the WT group, 2.7 ± 0.1 in the PBS group, and 6.5 ± 0.6 in the sEV group, with significantly lower numbers in the PBS and sEV groups compared with the WT group and higher numbers in the sEV group than the PBS group (Fig. 4H). The average soma areas in PRV-labelled motoneurons were different in the three groups; the soma area was largest in the WT group and smallest in the PBS, and the soma area of the sEV group was in the middle (Fig. 4I).

To accurately compare surviving motoneurons and their synaptic innervation, lumbar spinal sections were subjected to anti-ChAT and anti-synaptophysin double immunofluorescent staining and ChAT-positive motoneurons were counted in the unilateral ventral horn of lumbar spinal segments (Fig. 4D–F). The average ChAT-positive motoneurons per section were 20.5 ± 0.7 in the WT group, 7.3 ± 0.4 in the PBS group, and 14.1 ± 0.7 in the sEV group, with significant differences between the three groups (Fig. 4J). The average soma areas of ChAT-positive motoneurons were smaller in the PBS and sEV groups compared with the WT group, and they were larger in the sEV group compared with the PBS group (Fig. 4K). Presynaptic inputs on spinal motoneurons were identified by anti-synaptophysin labelling (Fig. 4d1–d3, e1–e3, f1–f3); synaptic coverage on individual motoneurons was (73.9 ± 2.3) % in the WT group, (35.0 ± 1.4) % in the PBS group, and (56.6 ± 1.7) % in the sEV group, with significant differences between groups (Fig. 4L). These results indicate that spinal motoneuron death, axon degeneration, and synaptic denervation occur in spinal cords of *SOD1*$^{G93A}$ mice and sEV administration effectively reduced these pathological changes.

### sEV administration facilitates preservation of electrophysiological function, myelin sheath, and NMJs in*SOD1*$^{G93A}$mice

Spinal motoneuron axons innervate skeletal muscles and form NMJs to drive muscle movement. In *SOD1*$^{G93A}$ mutant mice, paralysis first appeared in the hindlimbs. Therefore, we recorded EMG of gastrocnemius upon stimulating sciatic nerves in 20-week-old animals (Fig. 5A). The amplitude of EMG was significantly decreased in the PBS ((1.08 ± 0.19) mV) and sEV ((3.36 ± 0.30) mV) groups compared with the WT group ((6.90 ± 0.22) mV), and it was significantly increased in the sEV group compared with the PBS group (Fig. 5B). The EMG latency tended to be higher in the PBS group ((2.39 ± 0.21) ms) compared with the WT ((1.95 ± 0.20) ms) and sEV group ((2.14 ± 0.15) ms) but the difference was not significant (Fig. 5C). These results indicate sEV administration effectively reduces the decline in electrophysiological function of spinal motoneurons in *SOD1*$^{G93A}$ mice.

After EMG recordings, mouse sciatic nerves were collected for EM analysis. Compared with the WT group, in which the myelin sheath was well organized, axonal atrophy was readily identified in the PBS group by folded and wrinkled myelin sheath and separation of myelin sheath lamellae filled with disintegrating debris (Fig. 5D). In the sEV group, myelin sheath and axons were preserved much better than in the PBS group; some separation of axon membrane and myelin sheath innermost lamellae was visible. The G-ratio of myelin sheath was significantly increased in the PBS group compared with the WT and sEV groups, with no difference between the WT and sEV groups (Fig. 5E). These results indicate that sEV administration inhibits axon demyelination and degeneration in *SOD1*$^{G93A}$ mice.

NMJ changes were studied in the gastrocnemius by analyzing AchR clusters using α-BT staining (Fig. 5F). Many fragmented AchR clusters were identified in the PBS group, whereas rare and some clusters were seen in the WT and sEV groups, respectively. The average number of AchR clusters was significantly lower in the PBS group ((85 ± 4) clusters/section) compared with the WT group ((177 ± 3) clusters/section) and significantly higher

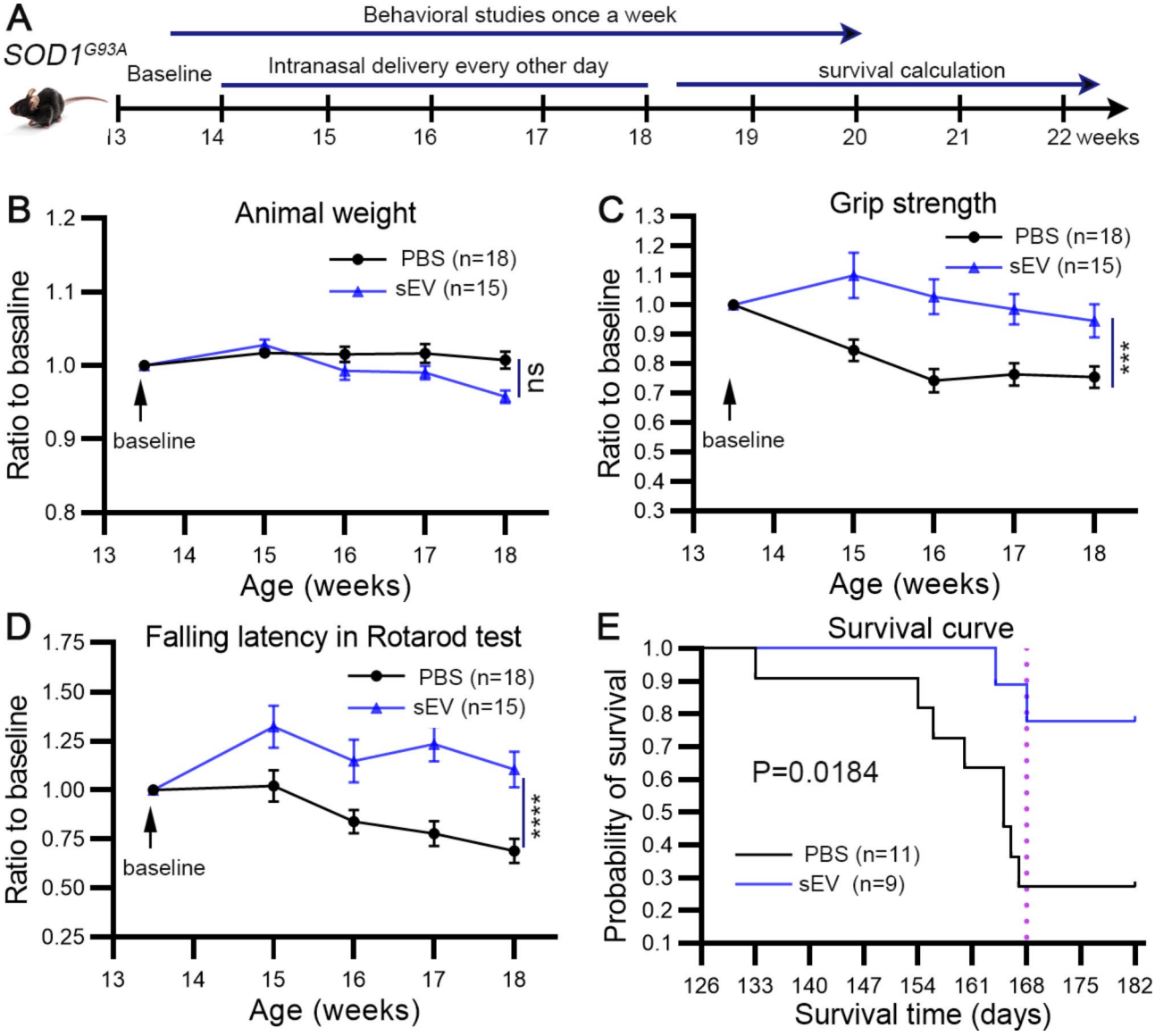


**Fig. 3** Intranasal administration of sEVs slows motor function decline and prolongs survival time in*SOD1*$^{G93A}$mice. **A**: Experimental workflow of the timepoints of sEV or PBS administration and data acquisition. Behavioral studies (animal weight, grip strength, and falling latency on the rotarod) were performed prior to administration and once a week thereafter. **B**: During the 4 weeks of administration, mouse body weight was comparable in the two groups. **C**: A decrease in grip strength was observed from 14 to 16 weeks in the PBS group, whereas there was a slight increase and then decrease to baseline in the sEV group. **D**: In the PBS group, the falling latency in the rotarod test gradually decreased from 15 weeks. In the sEV group, the falling latency slightly increased after one week of sEV administration and then was relatively stable; latency was significantly higher compared with that of the PBS group. E: Survival curves. The percentage of surviving animals at day 168 (24 weeks) (dotted red line) was 27% (8/11) in the PBS group and 78% (7/9) in the sEV group, indicating a significant increase of survival probability in the sEV group. ***$P < 0.001$; ****$P < 0.0001$; ns, not significant; two-way ANOVA multiple comparison in B–D; Gehan-Breslow-Wilcoxon test in **E**

in the sEV group ((127 ± 7) clusters/section) compared with the PBS group (Fig. 5G). The percentage of fragmented AchR clusters was higher in the PBS group ((32.3 ± 5.8) %) than in the WT ((2.5 ± 1.0) %) and sEV ((11.6 ± 2.2) %) groups (Fig. 5H). The average areas of AchR cluster surfaces showed opposite changes in the three groups (in $\mu m^2$: 3286 ± 48 in the WT group, 1789 ± 107 in the PBS group, 2988 ± 255 in the sEV group) (Fig. 5I).

### sEV administration alleviates mitochondrial damage of motoneurons in *SOD1*$^{G93A}$mice

Mitochondrial damage is an important pathological characteristic of human ALS patients and ALS animal models and is closely related to excitotoxicity, apoptosis, and cell survival. To evaluate the effect of sEV administration on mitochondria, we performed EM studies of spinal ventral horns from 20-week-old mice. In the WT animals, most mitochondria were observed in the cytoplasm of spinal

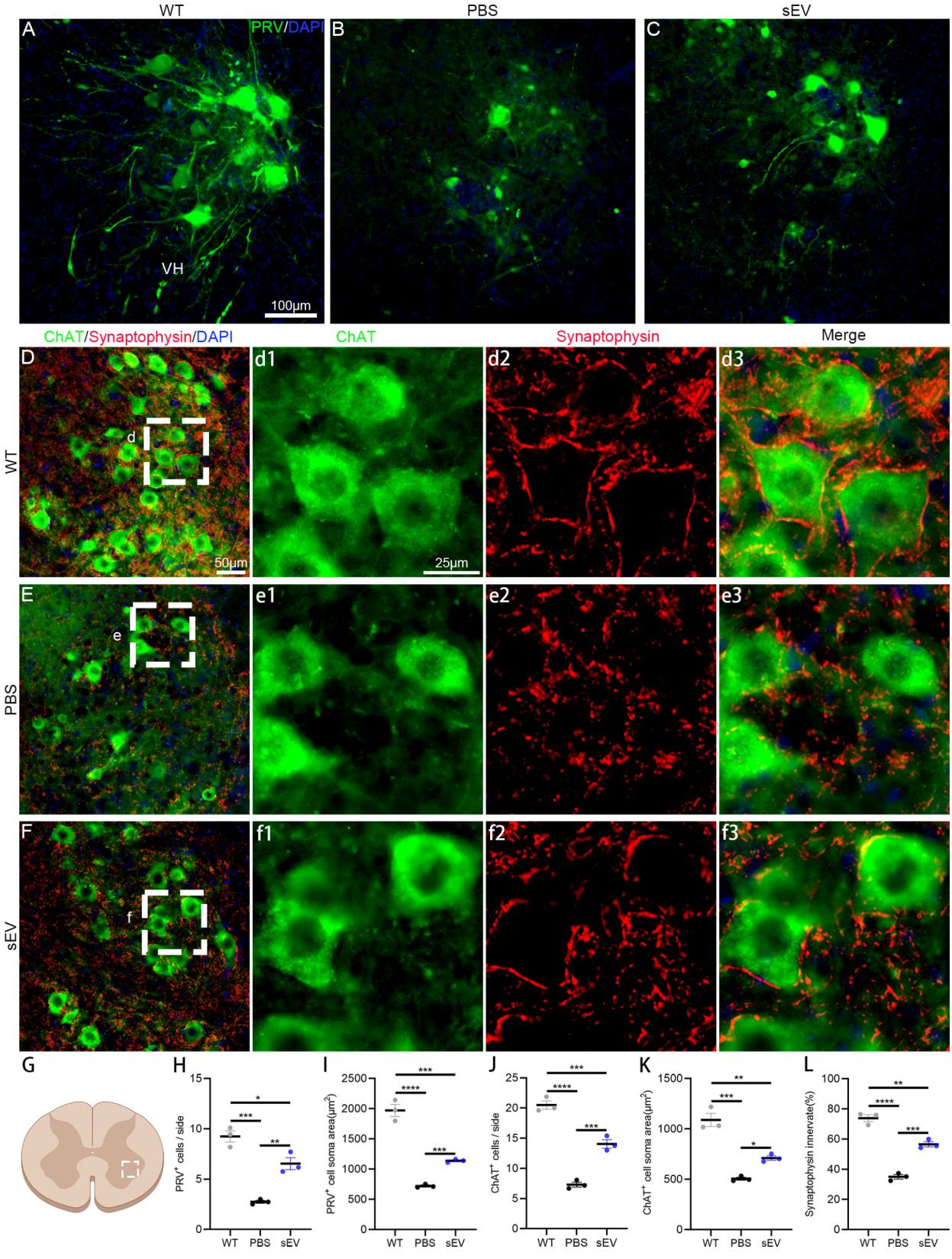


**Fig. 4** (See legend on next page.)

(See figure on previous page.)

**Fig. 4** sEV administration delays motoneuron degeneration and synaptic denervation in *SOD1*$^{G93A}$ mice. **A**–**C**: PRV injection into sciatic nerves retrogradely labeled lumbar spinal motoneurons in the WT (**A**), PBS (**B**), and sEV groups (**C**). **D**–**F**: Anti-ChAT (green) and anti-synaptophysin (red) double immunofluorescent staining showed spinal motoneurons and presynaptic coverage on spinal motoneurons in the WT (D, d1–d3), PBS (E, e1–e3) and sEV groups (F, f1–f3). Enlarged images in d1–d3, e1–e3, and f1–f3 are from the region indicated by the white dotted line in **D**, **E**, and **F**, respectively. G–L: In the unilateral ventral horn of spinal cord (selected region in the schema, **G**), statistical analysis showed significant differences in PRV-labelled motoneuron density (**H**) and average soma area (**J**), ChAT-positive motoneuron density (**J**) and average soma area (**K**), and the percentage of synaptophysin coverage on motoneurons among the three groups. *$P < 0.05$; **$P < 0.01$; ***$P < 0.001$; ****$P < 0.0001$; one-way ANOVA multiple comparison; $n = 3$ mice in each group and 12–15 slides/mouse

motoneurons with oblong or oval shapes, and mitochondrial cristae were evenly distributed and attached by many high-density particles (Fig. 6A, A'). In the PBS group, the morphology of mitochondria was completely deformed, showing swelling and round shapes, and a few cristae were identified in mitochondrial lumens (Fig. 6B, B'). In the sEV group, some mitochondria also showed swelling, but the mitochondrial cristae and particles were still preserved (Fig. 6C, C').

To further examine the changes of mitochondrial morphology, we measured the surface areas, circumferences, longitudinal and transverse diameters, and the areas filled with cristae in the mitochondrial lumens of all mitochondria in two well-identified motoneurons in each sample (3 animals in each group). The average surface areas of mitochondria were (in $\mu m^2$) 0.203 ± 0.013 in the WT group, 0.237 ± 0.005 in the PBS group, and 0.248 ± 0.006 in the sEV group, and there was a significant increase in the PBS and sEV groups compared with the WT group (Fig. 6D). The mitochondrial cristae areas were also measured separately (in $\mu m^2$): 0.0525 ± 0.0006 in the WT, 0.0174 ± 0.0002 in the PBS, and 0.0284 ± 0.0003 in the sEV, showing the significant differences among three groups (highest in the WT, middle in the sEV, and lowest in the PBS; Fig. 6E). The mitochondrial circumferences were increased in the PBS and sEV groups compared with the WT group (in μm): 1.901 ± 0.034 in the WT group, 2.456 ± 0.030 in the PBS group, and 2.218 ± 0.034 in the sEV group; the circumference was smaller in the sEV group compared with the PBS group (Fig. 6F). The changes of these parameters indicate the pathological characteristics of mitochondria in mutant mice. The aspect ratios of mitochondrial diameters were 1.883 ± 0.036 in the WT group, 1.382 ± 0.010 in the PBS group, and 1.745 ± 0.025 in the sEV group, with a significant increase in the WT and sEV groups compared with the PBS group and no differences between the WT and sEV groups (Fig. 6G). Mitochondrial swelling was associated with the loss of mitochondrial cristae and the vacuolation ratios (%) were 8.470 ± 0.306 in the WT group, 42.191 ± 0.635 in the PBS group, and 18.16 ± 0.553 in the sEV group. The vacuolation ratio was significantly higher in the PBS group than in the WT and sEV groups, and the ratio was significantly lower in the sEV group compared with the PBS group (Fig. 6H). These results suggest that sEV administration effectively alleviates mitochondrial damage of spinal motoneurons in the pathological progression of ALS in mice.

### sEV administration alleviates neuroinflammation in mutant spinal cords

Neuroinflammation is another important pathological feature in ALS progression. After 4 weeks of intervention in *SOD1*$^{G93A}$ mice, we collected spinal samples (lumbar enlargement segments) for cytokine detection. Among the eight cytokines examined, the expression levels of TNF-α, IFN-γ, and IL-10 were relatively consistent in mice in the same groups ($n = 3$/group) and were higher in the PBS group compared with the WT and sEV groups (Fig. 7A). Quantitative analysis revealed the expression levels (in pg/mL) in the three groups (WT, PBS and sEV): TNF-α (91.55 ± 5.16, 113.90 ± 1.92, and 96.72 ± 5.65), IFN-γ (10.95 ± 0.68, 14.39 ± 0.44, and 12.02 ± 0.20), IL-2 (5.93 ± 2.46, 4.85 ± 0.13, and 5.23 ± 0.82), IL-4 (0.47 ± 0.17, 0.80 ± 0.15, and 0.31 ± 0.06), IL-5 (0.38 ± 0.05, 0.57 ± 0.09, and 0.37 ± 0.01), IL-10 (2.43 ± 0.44, 3.55 ± 0.14, and 1.83 ± 0.05), KC (0.97 ± 0.03, 1.35 ± 0.30, and 0.87 ± 0.13), and IL-12p70 (49.74 ± 16.75, 91.97 ± 13.26, and 42.54 ± 6.89). There were significantly higher levels of TNF-α and IFN-γ in the PBS group compared with the WT group (Fig. 7B), indicating a neuroinflammatory response in mutant animals. In contrast, the expression levels of TNF-α, IFN-γ, IL-4, IL-10, and IL-12p70 were significantly downregulated in the sEV group compared with the PBS group (Fig. 7B).

To further confirm the neuroinflammatory changes in spinal cords, cervical spinal sections were subjected to immunofluorescent staining against Iba1 (for microglia) and GFAP (for astrocytes). In the WT group, Iba1-positive cells were evenly distributed in the white and grey matter (Fig. 7C), with small somas and many branches (Fig. 7c1–c3). In the PBS group, increased Iba1-positive cells accumulated in the grey matter, particularly in the ventral horn (Fig. 7D), and these cells showed enlarged somas and shortened branches (Fig. 7d1–d3). In the sEV group, fewer Iba1-positive cells and smaller somas were identified in the ventral horn compared with the PBS group (Fig. 7E). The microglia density in the ventral horn was significantly higher in the PBS group ((566 ± 22) cells/$mm^2$) than in the WT group ((98 ± 3) cells/$mm^2$) and the sEV group ((216 ± 18) cells/$mm^2$) and slightly higher in the sEV group than in the WT group (Fig. 7F).

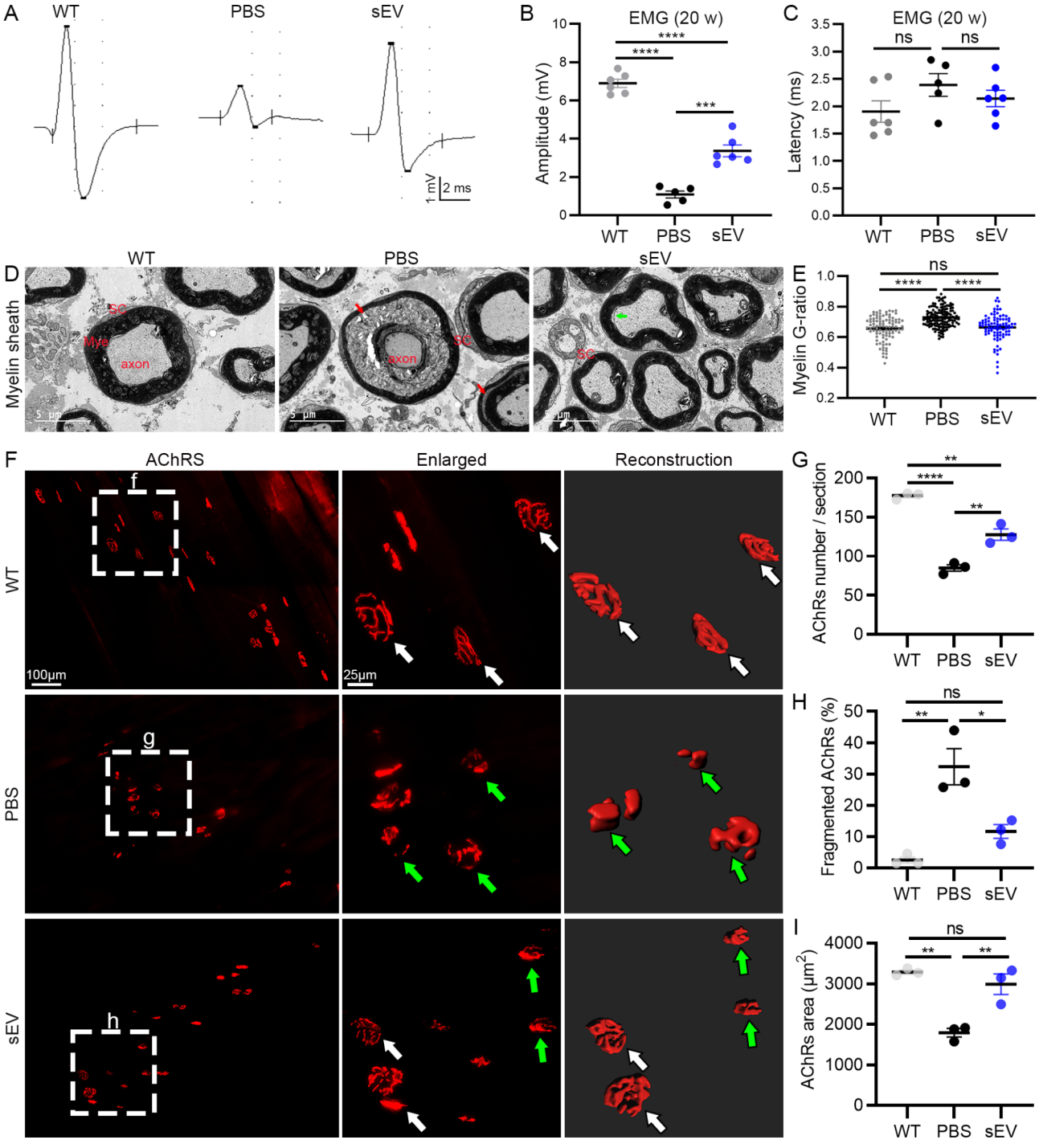


**Fig. 5** sEV administration facilitates preservation of electrophysiological function, NMJ AchRs, and myelin sheath in*SOD1*$^{G93A}$mice. **A**–**C**: Representative EMG recordings of gastrocnemius in the three groups (**A**); significant differences were observed in amplitude among the three groups (**B**), but no differences were observed in the EMG latency (**C**). **D**, **E**: EM studies of sciatic nerves showed myelin sheath separation (red arrows) and axon atrophy in the PBS group and early myelin sheath separation in the sEV group (green arrow) but not the WT group (**D**). A significant increase of G-ratio was observed in the PBS group compared with the WT and sEV groups, but no difference was observed between the WT and the sEV groups (**E**). **F**–**I**: AchR clusters in the gastrocnemius were observed by α-BT staining. Clusters were well preserved (white arrows) in the WT group. Many clusters were fragmented (green arrows) in the PBS group. In the sEV group, some AchR clusters were well preserved (white arrows) and some were fragmented (green arrows). Statistical analysis showed significant differences in the average AchR cluster numbers (**G**), the fragmented AchR cluster percentages (**H**), and the average AchR cluster surface areas (**I**) in the PBS group compared with the WT and sEV groups. *$P<0.05$; **$P<0.01$; ***$P<0.001$; ****$P<0.0001$; ns, not significant; one-way ANOVA multiple comparison; $n=5$ or 6 mice/group for EMG recordings and 3 mice/group for EM study and α-BT staining

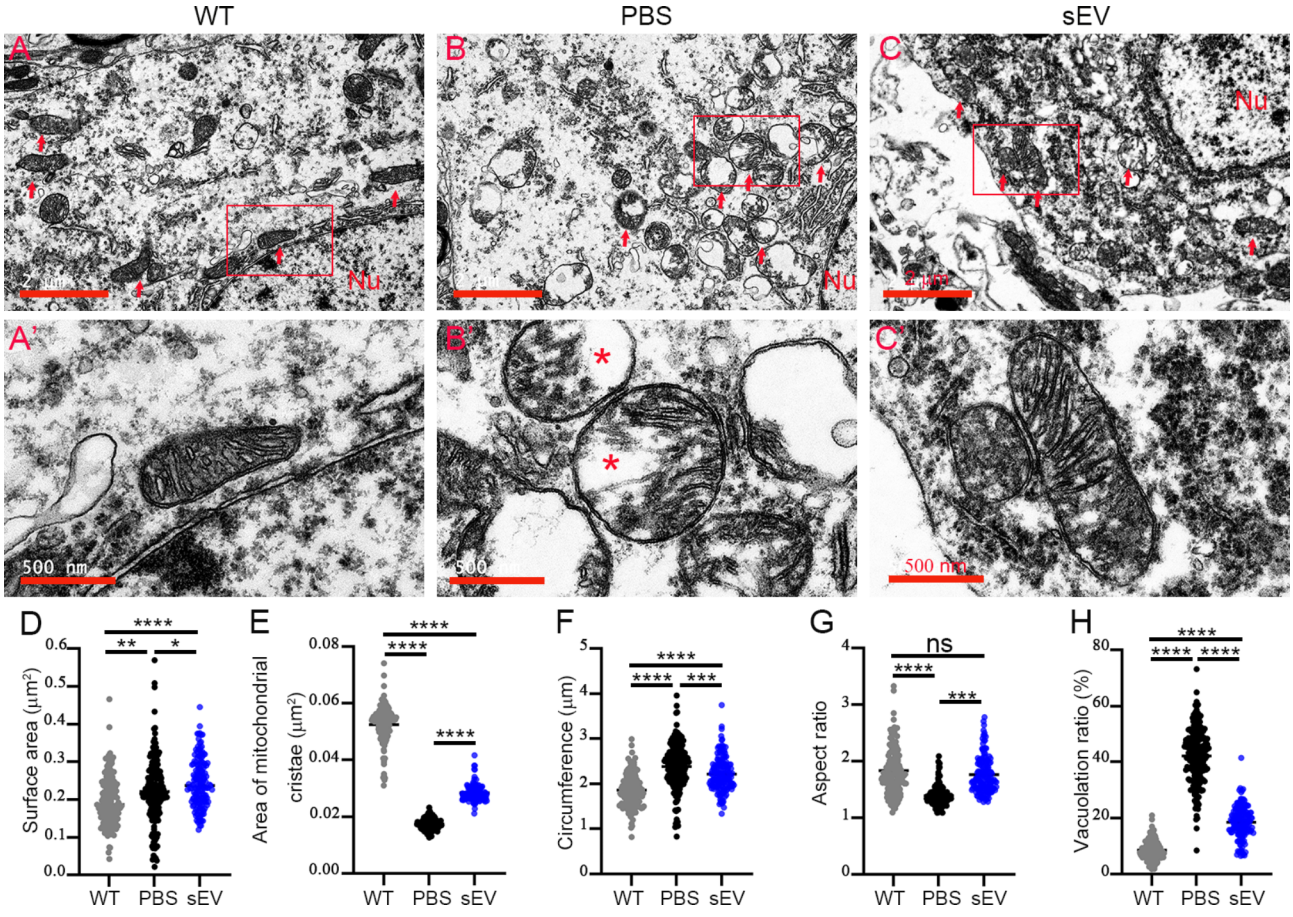


**Fig. 6** sEV administration alleviates mitochondrial damage of spinal motoneurons in*SOD1*$^{G93A}$mice. **A**–**C**: EM images of spinal motoneurons from 20-week-old mice in the WT (**A**), PBS group (**B**), and the sEV groups (**C**). Mitochondria were indicated by red arrows. A'–C' are higher magnification images from the selected regions in A–C, showing individual mitochondria. Nu, nucleus. D–H: Statistical analysis of total mitochondrial surface areas (**D**), mitochondrial cristae areas (**E**), circumferences **F**), aspect ratios (**G**), and vacuolation rations (**H**) in the WT, PBS, and sEV groups. **P* < 0.05; ***P* < 0.01; ****P* < 0.001; *****P* < 0.0001; ns, not significant; one-way ANOVA multiple comparison; 80–150 mitochondria/neuron, 2 neurons/mouse, and 3 mice in each group for analysis

Similarly, an increased astrocyte response was identified in the PBS group compared with the WT group, and this was decreased in the sEV group compared with the PBS group (Fig. 7G–I). The density of astrocytes in the ventral horn was significantly higher in the PBS group ((1116 ± 62) cells/mm$^2$) than in the WT ((404 ± 16) cells/mm$^2$) and sEV groups ((625 ± 28) cells/mm$^2$) (Fig. 7J).

### sEV administration inhibits overactivation of complement-coagulation cascade and NF-κB signaling pathways in *SOD1*$^{G93A}$mice

To decode the mechanism underlying effects of sEVs in ALS mice, we collected lumbar spinal samples from the WT, PBS, and sEV groups (after 4 weeks of intervention) at the age of 18 weeks and performed proteomics analysis. A total of 839 DEPs were identified in the PBS (mutant) group compared with the WT group, including 506 upregulated DEPs and 333 downregulated DEPs (FDR < 0.05, foldchange > 1.5) (Fig. 8A). KEGG analysis showed that 26 DEPs were clustered in the complement and coagulation cascade (the top pathway) and 14 DEPs were clustered in the NF-κB signaling pathway (the top 19th pathway) (Fig. 8C). The complement and coagulation cascades were significantly overactivated in GSEA in the PBS group compared with the WT (normalized enrichment score = 2.63, FDR < 0.00001) (Fig. 8E). All 26 DEPs in the complement and coagulation cascade, including C1q, C3, C4b, Serpina1, Serpind1, Serping1, Plg, Itgb2, Itgam, A2m, F3, Clu, Cfd, Vtn, Cfi, Cfh, Fga, Fgb, and Fgg, were significantly increased in the PBS group (Fig. S4A). Overactivation of the NF-κB signaling pathway was also found in the PBS group compared with the WT (normalized enrichment score = 1.92, FDR < 0.01) (Fig. 8G). Among the 14 DEPs in the NF-κB signaling pathway, 12 DEPs (Nfkb2, Vcam1, Icam1, Irak4, Ddx58, Plcg2, Parp1, Lyn, Cd14, Trim25, Ighg2b, and Ighm) were upregulated and 2 DEPs (Traf3 and Tab3) were downregulated (Fig. S4B). In addition, regulation of

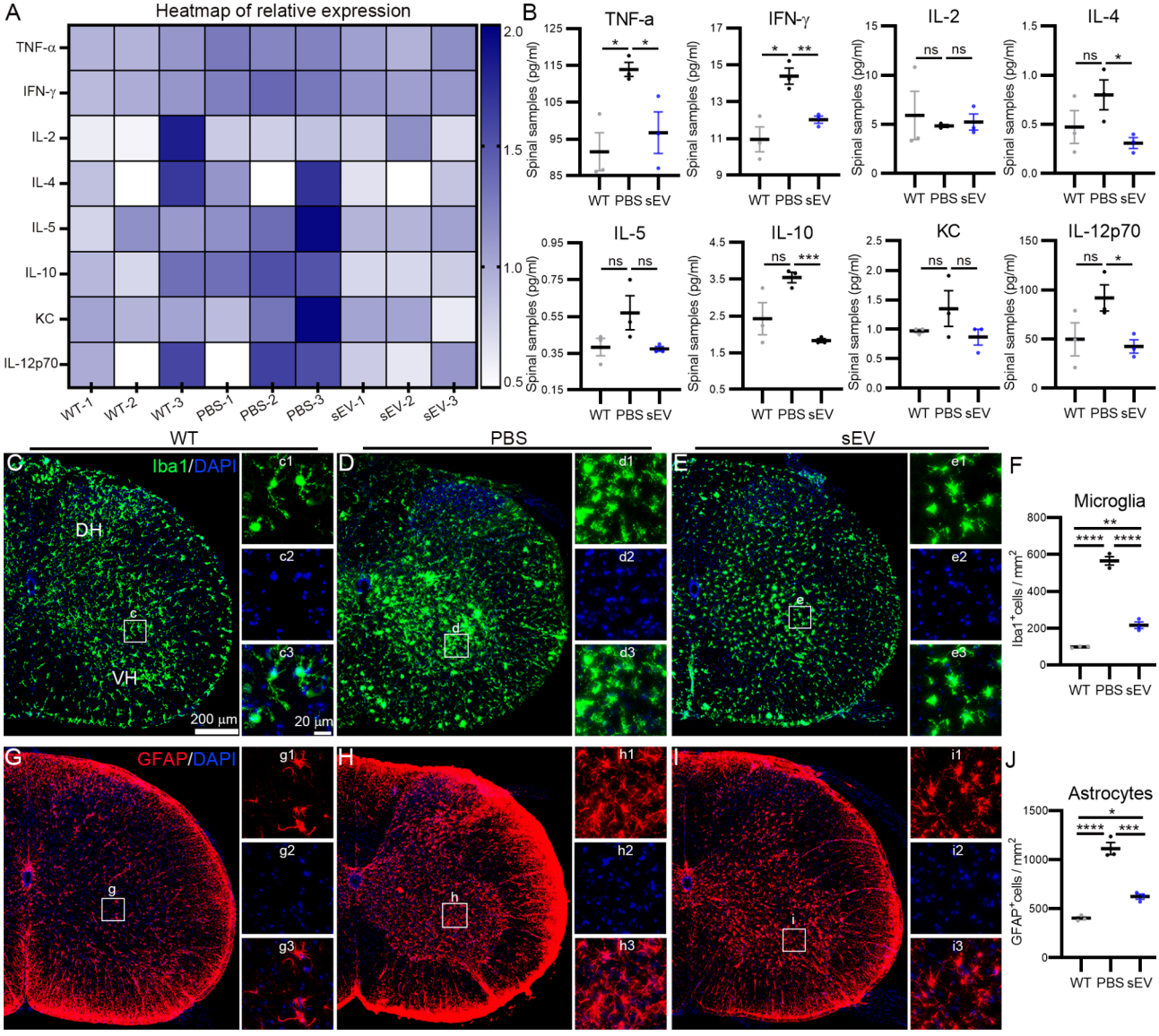


**Fig. 7** sEV administration alleviates neuroinflammation in the spinal cord of *SOD1*$^{G93A}$mice. **A**, **B**: Cytokines were analyzed in lumbar spinal samples after 4 weeks of intervention. Heatmap of the relative expression of cytokines in individual samples (**A**). Quantitative analyses identified a significant upregulation of TNF-α and IFN-γ in the PBS group compared with the WT group and a significant downregulation of TNF-α, IFN-γ, IL-4, IL-10, and IL-12p70 in the sEV group compared with the PBS group (**B**). **C**–**F**: Anti-Iba1 immunostaining showed microglial cells in transverse cervical spinal sections from the WT (**C**), PBS (**D**), and sEV groups (**E**). Images in selected regions of three groups were enlarged to identify microglial morphology in the corresponding left panels. Cell densities in the ventral horn were higher in the PBS group than the WT and sEV groups and slightly higher in the sEV group compared with the WT group (**F**). G–J: Astrocytes were analyzed by anti-GFAP immunostaining in the WT (G), PBS (H), and sEV groups (I); astrocyte morphology in the ventral horn (selected regions) was shown in enlarged images in the corresponding left panels. Cell density was higher in the PBS group than the WT and sEV groups and higher in the sEV group compared with the WT group (**J**). **P* < 0.05; ***P* < 0.01; ****P* < 0.001; *****P* < 0.0001; ns, not significant; one-way ANOVA multiple comparison; 3 mice in each group. DH, dorsal horn; VH, ventral horn

actin cytoskeleton was identified as one of top 20 pathways in KEGG analysis of DEPs between the PBS group and the WT group (Fig. 8C), and 30 DEPs were clustered in this pathway including 23 DEPs (Igtb2, Itga5, Actn1, Itga2, Egfr, Iqgap2, Vcl, Myh9, Nckap1l, Itgb5, Myl12a, Itga7, Itgb1, Fn1, Arpc1b, Iqgap1, Pak4, Itgam, Msn, Vav1, Fgf2, Ezr, Gm49368) with upregulation and 7 DEPs (Pfn2, Limk1, Fgf1, Cfl2, Kras, Chrm2, Mylpf) with downregulation in the PBS group.

We also identified 91 DEPs in the sEV group compared with the PBS group, including 46 upregulated DEPs and 45 downregulated DEPS (FDR < 0.05, foldchange > 1.5) (Fig. 8B). KEGG analysis showed that the complement and coagulation cascade (11 DEPs, top 1st pathway) and the NF-κB signaling pathway (5 DEPs, top 20th pathway)

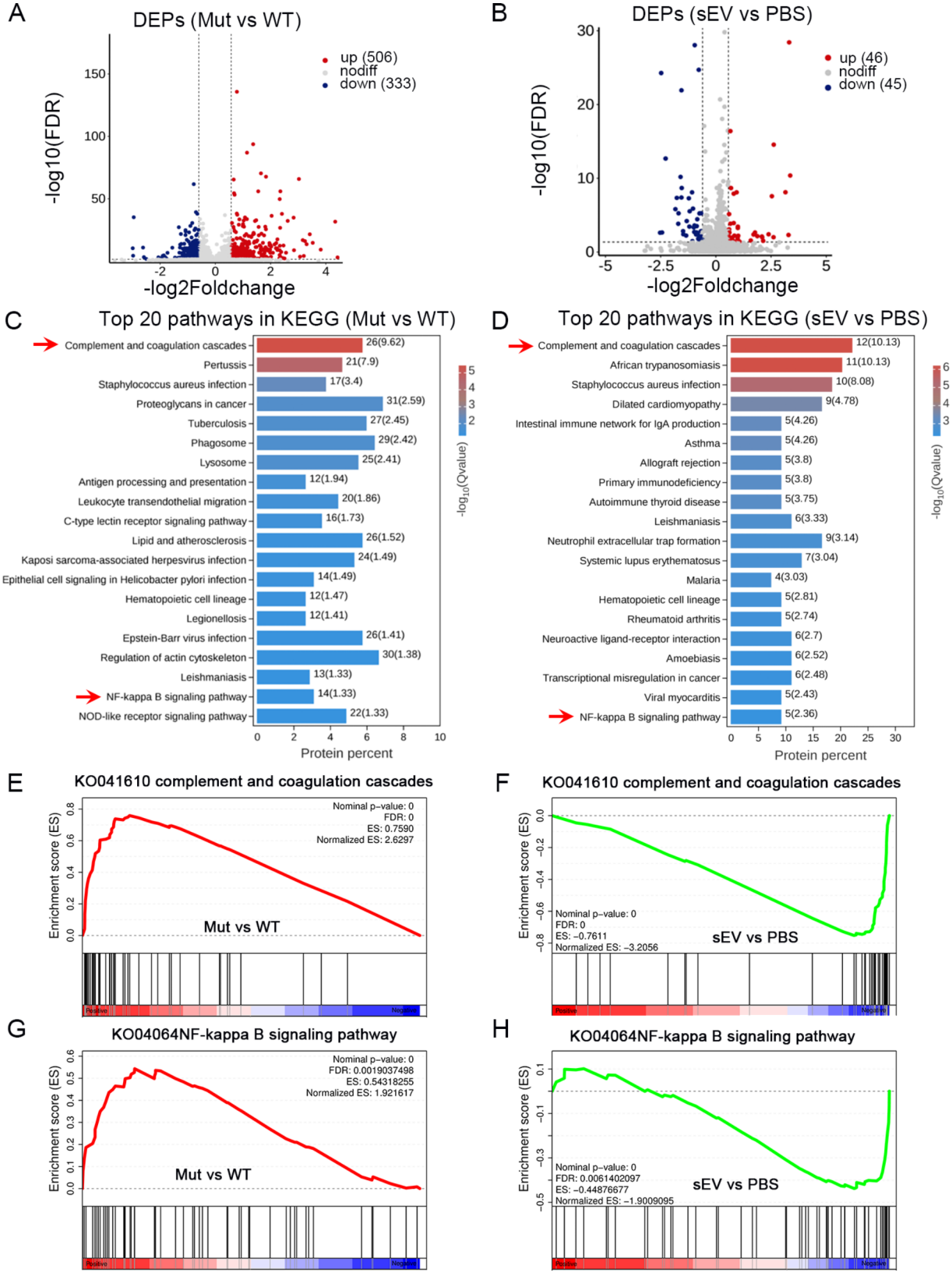


**Fig. 8** (See legend on next page.)

(See figure on previous page.)

**Fig. 8** Proteomic profiling of spinal cord samples in $SOD1^{G93A}$ mice after sEV administration. **A**, **B**: Volcano plots of differentially expressed proteins (DEPs) using protein mass spectrometry analysis of spinal cord samples in the mutant (Mut) group (namely the PBS group) versus the WT group (**A**) and the sEV group versus the PBS group (**B**). **C**, **D**: KEGG analysis identified the top 20 pathways of DEPs between the mutant (Mut) group and the WT group (**C**) and between the sEV group and the PBS group (**D**). The complement and coagulation cascade and NF-κB signaling pathways were indicated by red arrows. E–H: GESA showed upregulation of the complement and coagulation cascade and NF-κB signaling pathway in the mutant group (Mut, namely the PBS group) compared with the WT group (**E**, **G**) and downregulation of the complement and coagulation cascade and NF-κB signaling pathways in the sEV group (sEV) compared with the PBS group (**F**, **H**). Three animals in each group were used for analyses

were significantly altered (Fig. 8D). These pathways were significantly downregulated in the sEV group compared with the PBS group in GSEA (Fig. 8F, H). All 11 DEPs in the complement and coagulation cascade (C3, C1q, Serpina1a, Serpina1b, Serpina1e, Kng1, Plg, Fga, Fgb, Fgg, and Cfd) and 5 DEPs in the NF-κB signaling pathway were decreased in the sEV group (Fig. S4C, D). Regulation of actin cytoskeleton was not identified as among the top 20 pathways in KEEG analysis of DEPs between the sEV and the PBS group.

Western blots of spinal samples also showed a significant upregulation of C1q and NF-κB in the PBS group compared with the WT group. Both C1q and NF-κB were significantly downregulated in the sEV group compared with the PBS group (Fig. S5).

To examine whether changes of these signaling pathways also happen at the transcriptional level, cervical spinal samples from the same animals used for proteomics analysis were subjected to RNAseq. The results showed 1438 DEGs including 1112 upregulated DEGs and 326 downregulated DEGs in the PBS group compared with the WT group (Padj < 0.05, foldchange > 2) (Fig. 9A). The complement and coagulation cascade and NF-κB signaling pathways were among the top 20 pathways in the KEGG analysis of the total DEGs (Fig. 9B). Furthermore, 18 DEGs (including *C1q*, *C3*, *C4b*, *Serpine1*, *F9*, and *Itgam*) in the complement and coagulation cascade were significantly upregulated in the PBS group compared with the WT group (Fig. 9C). In the PBS group, 22 DEGs were clustered in the NF-κB signaling pathway, including 1 downregulated DEG (*Card10*) and 21 upregulated DEGs (including *Nfkb2* and *Bcl2*) (Fig. 9D). The results also showed 26 DEGs including 3 upregulated DEGs (*Igsf9b*, *Lars2*, and *Gm23935*) and 23 downregulated DEGs in the sEV group compared with the PBS group (Padj < 0.05, foldchange > 1.5) (Fig. 9E, F). Among the 23 downregulated DEGs, 6 DEGs (*C1qtnf7*, *C2*, *C1qtnf1*, *Serpina1e*, *Serpina3h*, and *Serpina9*) were involved in the complement and coagulation cascade and 2 DEGs (*Bcl2l14* and *Bcl2l1*) were related to the NF-κB signaling pathway. The other 15 downregulated DEGs were *Ptgs2*, *Sult1a1*, *Xdh*, *Pnpla2*, *Plin4*, *Fkbp5*, *Fam214a*, *Dpep1*, *Zfand4*, *Hif3a*, *Card14*, *Sgk3*, *Tmem53*, *Fmo2*, and *Pla2g3* (Fig. 9F).

Together, the proteomic and transcriptomic data demonstrated that the complement and coagulation cascade and NF-κB signaling pathways were overactive in the spinal cords of $SOD1^{G93A}$ mice, and sEV administration alleviated activation of these signaling pathways.

## Discussion

ALS is an irreversible disease of progressive motoneuron degeneration, and the current therapeutic strategies focus on delaying pathological progression and skeletal muscle paralysis. In the present work, we demonstrate that intranasal delivery of MSC-derived sEVs is a promising intervention for ALS therapy. First, sEV administration improved motor function and prolonged survival time of ALS transgenic mice. Second, the pathological changes of ALS mice were significantly improved after sEV treatment, including motor neuron loss, mitochondrial impairment, axon demyelination, synaptic denervation, NMJ degeneration, and EMG deficits. Third, sEV administration effectively alleviated neuroinflammation by inhibiting proinflammatory cytokine production and overactivation of complement-coagulation cascade and NF-κB signaling pathways. These findings will contribute to developing a flexible (e.g., intranasal delivery) and non-cellular therapeutic strategy for ALS.

Drug delivery to the CNS is a challenge because of the BBB, which makes it difficult for transplanted cells and drugs with high molecular weight to enter the brain parenchyma after intravenous delivery. Intranasal delivery is an alternative strategy to overcome this difficulty, and the cargos of sEVs can be transported from the nasal cavity to the CNS by the olfactory nerves or the connective tissues surrounding the olfactory bundles [28]. After intranasal administration in $SOD1^{G93A}$ mice, sEVs extensively entered the CNS and were taken up by numerous neurons and some microglial cells. In spinal motoneurons and interneurons, abundant sEV nanoparticles were visible, indicating that the sEVs were successfully transported. Because of their small size, sEVs can also be transported to the CNS upon intravenous administration [23]. Our recent study showed that intranasal delivery effectively increases sEV accumulation in the damaged CNS and reduces sEV distribution in other organs such as the liver and lungs, reducing side effects [24]. In line with this, we did not observe any morphological changes of the liver, spleen, and kidney in $SOD1^{G93A}$ mice after 4 weeks of intranasal administration of sEVs.

Stem cell–based therapy is a desirable candidate for ALS treatment. Stem cells play multifaceted roles by potentially targeting multiple pathogenic mechanisms

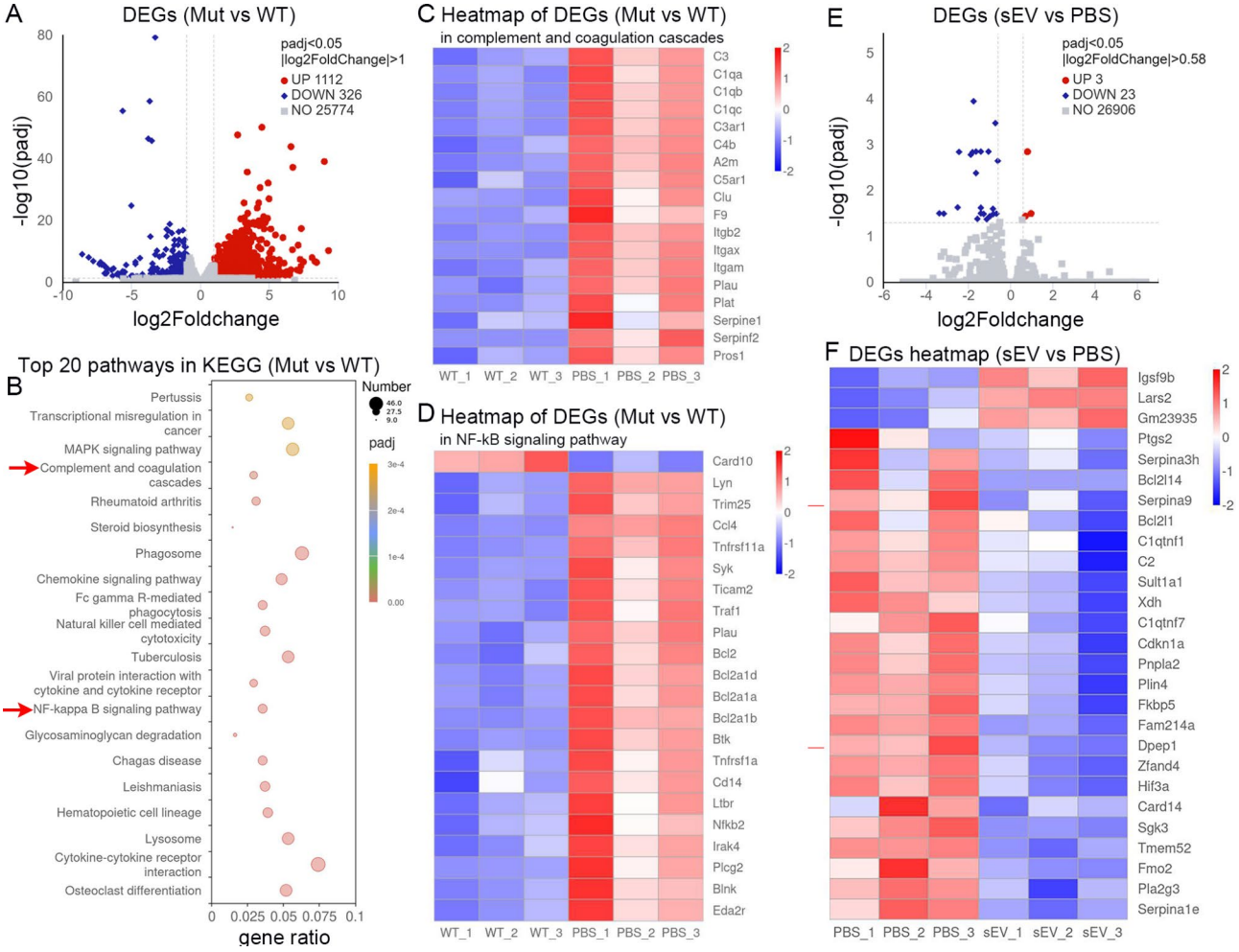


**Fig. 9** Transcriptomic profiling of spinal cord samples in *SOD1*$^{G93A}$ mice after sEV administration. **A**, **E**: Volcano plots of differentially expressed genes (DEGs) identified by RNAseq of spinal cord samples in the mutant group (PBS group) compared with the WT group (**A**) and the sEV group compared with the mutant group (**E**). **B**: KEGG analysis of the top 20 pathways of DEGs between the mutant group and the WT group. The complement and coagulation cascade and NF-κB signaling pathways were indicated by red arrows. C, D: Heatmaps of DEGs clustered in the complement and coagulation cascade (**C**) and the NF-κB signaling pathways (**D**) in the mutant group and the WT group. **F**: Heatmap of DEGs between the sEV group and the PBS group. Three animals in each group were analyzed

such as neuroprotection, anti-inflammation, and immunomodulation mechanisms. The first phase I clinical trial for stem cell-based therapy was approved by FDA in 2009; however, this approach is not a satisfactory, reliable clinical option [29]. The effectiveness of stem cell treatment for ALS is affected by many factors including how extensively the transplanted stem cells penetrate into brain parenchyma, cell survival, and transplantation route. sEVs contain multiple biologically active molecules from the stem cells, such as nucleic acids and proteins, and a study showed that sEVs exhibited the same therapeutic effects as stem cells in the treatment of cerebral ischemia [30]. Our study shows that intranasal delivery of sEVs overcomes many issues of stem cell transplantation and delayed disease progression of ALS in *SOD1*$^{G93A}$ mice. The onset of behavioral symptoms in *SOD1*$^{G93A}$ mice started as early as 14 weeks old. Thereafter, a gradual decline in motor capacity was observed, as shown in grip strength and rotarod tests. Starting from the symptom onset, 4 weeks of administration of sEVs decreased the progressive decline of motor function and prolonged the survival time of mutant mice.

Motor function decline in the ALS mouse model is directly attributed to progressive motoneuron atrophy and loss, which was confirmed by a PRV tracing study and anti-ChAT immunostaining in the PBS group. The pathological change was accompanied by presynaptic denervation on dying spinal motoneurons (anti-synaptophysin immunostaining), motoneuron axon demyelination (EM study), NMJ degeneration (α-BT immunostaining), and electrophysiological function impairment (EMG recordings). Intranasal administration of sEVs significantly alleviated these pathological changes compared with the PBS group, with increased surviving

spinal motoneurons, improved presynaptic and myelin sheath preservation, better preserved AchR clusters, and higher EMG amplitude. These morphological and electrophysiological results support the behavioral improvements in the sEV group. These results indicate that intranasal administration of sEVs exerts a therapeutic effect on ALS. Cytoskeleton disruption of spinal motoneurons is an important cause of progressive neuronal death during the ALS progression. We identified 30 DEPs between the PBS group and the WT group clustered in regulation of actin cytoskeleton (Top 17th pathway). It is reported that disruption of the neuronal actin barrier induced by repulsive guidance molecule A (RGMa) as the important pathological mechanism of the ALS progression and administration of anti-RGMa antibodies is supposed to be an effective therapeutic strategy for ALS [31]. However, regulation of actin cytoskeleton was not identified as among top 20 pathways in KEEG analysis of DEPs between the sEV and the PBS group. Whether sEVs impose a direct effect on regulation of actin cytoskeleton is required for further study.

Oxidative stress, mitochondrial dysfunction, and neuroinflammation are the important pathological mechanisms for motoneuron damage during ASL progression [6]. In the PBS group, numerous mitochondria in spinal motoneurons underwent vacuolation and degeneration, identified by EM, and these changes were alleviated after 4 weeks of sEV treatment. During the pathological process, the total mitochondrial surface area increases initially and then decreases due to many cristae loss [32, 33]. The higher total surface area of mitochondria in the sEV group than the PBS group indicates sEV administration delays the degeneration and loss of mitochondrial cristae. This is also supported by differences of mitochondrial cristae areas in three groups (highest in the WT, middle in the sEV, and lowest in the PBS).

The overall immunoregulatory imbalance of pro-inflammation and anti-inflammation is a contributor to ALS development [34]. Our data showed that sEV administration significantly downregulated the expression of both Th1 pro-inflammatory cytokines (TNF-a, IFN-γ, IL-12p70) and Th2 anti-inflammatory cytokines (IL-4 and IL-10) compared to the PBS group, and these cytokines showed a significant increase (TNF-a, IFN-γ) or an increase trend (IL-4, IL-10, and IL-12p70) in the PBS group compared to WT animals. Pro-inflammatory cytokines (TNF-a, IFN-γ, IL-12p70) were expressed at higher levels than anti-inflammatory cytokines (IL-4 and IL-10). Our results are consistent with the previous reports that the levels of most individual Th1 and Th2 cytokines are generally higher in $SOD1^{G93A}$ mutant mice than the corresponding WT mice during ALS development [35]. Simultaneous downregulation of Th1 pro-inflammatory and Th2 anti-inflammatory cytokines predicts that sEV administration may promote immunoregulatory balance of pro-inflammatory and anti-inflammatory response, which should be beneficial for ALS treatment. In the mutant spinal cords, elevated neuroinflammation was also indicated by increased glial response, which was reduced after sEV administration. Pathological changes such as motoneuron damage, mitochondrial dysfunction, and neuroinflammation may reciprocally interplay to promote the progression of ALS, and sEV administration effectively reduced disease deterioration by alleviating these pathological responses.

Activation of the complement-coagulation cascade is an early component of neuroinflammation after brain injury, and inhibiting the cascade overshooting activation is a potential strategy to reduce neuron damage [36]. Overactivation of the complement-coagulation cascade and NF-κB signaling pathways may be important molecular mechanisms in pathological changes of ALS. The complement cascade is activated to form a membrane attack complex, which results in cell damage and inflammation. Abnormal activation of the complement-coagulation cascade has been reported in neurodegenerative diseases, with upregulation of complement molecules and coagulation molecules [37]. In traumatic brain injury, C3 activation triggers a sustained glial response, neuroinflammation, and neuronal damage [38]. Deletion or inhibition of the main components of the complement system alleviated neuroinflammation and neuron loss [39]. Proteomic analysis showed that the complement-coagulation cascade was the top pathway of the DEPs in the $SOD1^{G93A}$ mice and the pathways were remarkably upregulated in these mice compared with those in the WT group. All 25 main molecules in the complement-coagulation cascade were significantly upregulated in the PBS group compared with the WT group. Overactivation of the complement-coagulation cascade was also confirmed by RNAseq and western blots of spinal samples. Moreover, the complement-coagulation cascade was significantly downregulated in the $SOD1^{G93A}$ mouse spinal cords after 4 weeks of sEV administration as confirmed by proteomic analysis, transcriptomic study (RNAseq), and western blots. NF-κB signaling was upregulated in the PBS group compared with the WT group and significantly reduced after sEV administration. The NF-κB signaling pathway controls cytokine production and cell survival, and its activation promotes oxidative stress, mitochondrial dysfunction, and neuroinflammation [40]. These results suggest that sEVs inhibit the complement-coagulation cascade and NF-κB signaling to alleviate pathological changes of ALS. In line with our findings, prolonged survival of ALS mice was reported by downregulating PAR1, one complement molecule [41, 42].

Because sEVs are rich in diverse contents derived from stem cells, their therapeutic effects should be

combinatorial and multi-targeted. In addition to the DEGs in the above signaling pathways, many other DEGs closely related to the pathological progress of ALS were altered on sEV administration. For example, *Igsf9b* and *Lars2* were significantly downregulated in the sEV group compared with the PBS group. *Lars2* is a mitochondria-associated gene, and its upregulation contributes to maintaining mitochondrial function [43]. *Igsf9b* encodes an adhesion protein required for synaptic plasticity [44, 45]. *PLA2G3*, a downregulated DEG in the sEV group, is positively correlated with neurodegeneration and the encoded protein regulates oxidative stress [46]; *Fkbp5* encodes a protein that enhances neuroinflammation by activating the NF-κB signaling pathway [47]. How the cargos in sEVs trigger these signaling networks and which components in sEVs account for their exact effects requires further research. In our previous study, we identified multiple proteins and miRNAs in MSC-derived sEVs, and the top abundant miRNAs were involved in multiple signaling pathways including the immune and inflammatory processes [24]. The miRNAs in sEVs may exert their functions by transcriptional regulation in spinal host cells to slow down motoneuron degeneration, in line with the previous report [48].

There are still some limitations in our study. First, therapeutic effects of sEVs should be combinatory because they contain diverse contents, and the components in sEVs and their detailed functional mechanisms have not been decoded in the present work. Second, we started sEV administration at the symptom onset of ALS in mutant mice and did not study whether sEV administration was also effective at the later stage of ALS.

## Conclusions

sEVs significantly alleviate multiple pathological changes to delay the progression of ALS by inhibiting the complement-coagulation cascade and NF-κB signaling pathways. Intranasal administration of sEVs is a promising therapeutic strategy for ALS.

### Abbreviations

| | |
|---|---|
| AchR | Acetylcholine receptor |
| ALS | Amyotrophic lateral sclerosis |
| BBB | Brain-blood barrier |
| ChAT | Choline acetyltransferase |
| CNS | Central nervous system |
| EM | Electron microscopy |
| EMG | Electromyogram |
| NF-κB | Nuclear factor kappa-B |
| GFAP | Glial fiber acid protein |
| IFN-γ | Interferon-γ |
| iPSC | Induced pluripotent stem cell |
| MSC | Mesenchymal stem cell |
| NMJ | Neuromuscular junction |
| PBS | Phosphate buffered saline |
| RNAseq | RNA sequencing |
| PRV | Pseudorabies virus |
| ROS | Reactive oxygen species |
| sEV | Small extracellular vesicle |
| SOD1 | Cytoplasmic copper/zinc superoxide dismutase 1 |
| TNF-α | Tumor necrosis factor-α |
| WT | Wild type |

## Supplementary Information

The online version contains supplementary material available at https://doi.org/10.1186/s12951-024-02764-2.

Supplementary Material 1

### Acknowledgements

We wish to thank Meizhi Wang, Jongwe Qin, Jing Li, and Qingwen Mo for technical support.

### Author contributions

LBZ, QLF and WRQ designed the experiments; JRZ initiated the study; JRZ, FXL and BJ performed experiments and data analysis; ZHH, MTH and HDW cooperated in EMG recordings, tracing studies, western blots and data analysis; ZCW and QLF prepared and characterized MSC-derived sEVs; JRZ, FXL and BJ input data to the manuscript; LBZ edited the manuscript; and QLF, WRQ and KWS revised the manuscript. All authors have read and approved the final manuscript.

### Funding

This work was supported by the following grants: National Key R&D Program of China (2022YFA1104900, Q. Fu & L. Zhou), 2023 University Innovation and Entrepreneurship Training Plan (202310183302, J. Zhou), Guangdong Basic and Applied Basic Research Foundation (No. 2021B1515120062), and Guangzhou Key R&D Program (2023B03J1233, 20220600003).

### Data availability

Data is provided within the manuscript or supplementary information files.

## Declarations

### Ethics approval

Animal experimental procedures were approved by the Animal Ethics Committee of Jinan University (Approval No.: IACUC-20230831-09).

### Consent for publication

Not applicable.

### Competing interests

The authors declare no competing interests.

### Author details

[1]Department of Hand Surgery, The Second Hospital of Jilin University, Changchun 130041, P. R. China
[2]Key Laboratory of CNS Regeneration (Ministry of Education), Guangdong Key Laboratory of Non-human Primate Research, Guangdong-Hongkong-Macau CNS Regeneration Institute of Jinan University, Guangzhou 510632, P. R. China
[3]Otorhinolaryngology Hospital, The First Affiliated Hospital, Sun Yat-sen University, Guangzhou 510080, P. R. China
[4]Extracellular Vesicle Research and Clinical Translational Center, The First Affiliated Hospital, Sun Yat-sen University, Guangzhou 510080, P. R. China
[5]Co-innovation Center of Neuroregeneration, Nantong University, Nantong, Jiangsu, P. R. China
[6]Neuroscience and Neurorehabilitation Institute, University of Health and Rehabilitation Sciences, Qingdao, Shandong 266071, P. R. China
[7]Department of Neurology and Stroke Center, The First Affiliated Hospital & Clinical, Neuroscience Institute of Jinan University, Guangzhou 510632, P. R. China
[8]Center for Exercise and Brain Science, School of Psychology, Shanghai University of Sport, Shanghai 200438, P. R. China
[9]Guangdong-Hongkong-Macau CNS Regeneration Institute, Jinan University, Huangpu Avenue West 601, Guangzhou 510632, P. R. China

[10]Otorhinolaryngology Hospital, Extracellular Vesicle Research and Clinical Translational Center, The First Affiliated Hospital, Sun Yat-sen University, Zhongshan Road II 58, Guangzhou 510080, P. R. China

Received: 19 March 2024 / Accepted: 12 August 2024
Published online: 22 August 2024

**References**

1. van Es MA, Hardiman O, Chio A, Al-Chalabi A, Pasterkamp RJ, Veldink JH, van den Berg LH. Amyotrophic lateral sclerosis. Lancet. 2017;390:2084–98.
2. Cleveland DW, Rothstein JD. From Charcot to Lou Gehrig: deciphering selective motor neuron death in ALS. Nat Rev Neurosci. 2001;2:806–19.
3. Rosen DR, Siddique T, Patterson D, Figlewicz DA, Sapp P, Hentati A, Donaldson D, Goto J, O'Regan JP, Deng HX, et al. Mutations in Cu/Zn superoxide dismutase gene are associated with familial amyotrophic lateral sclerosis. Nature. 1993;362:59–62.
4. Brenner D, Freischmidt A. Update on genetics of amyotrophic lateral sclerosis. Curr Opin Neurol. 2022;35:672–7.
5. Zhang S, Cooper-Knock J, Weimer AK, Shi M, Moll T, Marshall JNG, Harvey C, Nezhad HG, Franklin J, Souza CDS, et al. Genome-wide identification of the genetic basis of amyotrophic lateral sclerosis. Neuron. 2022;110:992–e10081011.
6. Bonafede R, Mariotti R. ALS Pathogenesis and Therapeutic approaches: the role of mesenchymal stem cells and extracellular vesicles. Front Cell Neurosci. 2017;11:80.
7. Jaiswal MK. Riluzole but Not Melatonin ameliorates Acute Motor Neuron Degeneration and moderately inhibits SOD1-Mediated Excitotoxicity Induced disrupted mitochondrial ca(2+) signaling in amyotrophic lateral sclerosis. Front Cell Neurosci. 2016;10:295.
8. Witzel S, Maier A, Steinbach R, Grosskreutz J, Koch JC, Sarikidi A, Petri S, Gunther R, Wolf J, Hermann A, et al. Safety and Effectiveness of Long-Term Intravenous Administration of Edaravone for treatment of patients with amyotrophic lateral sclerosis. JAMA Neurol. 2022;79:121–30.
9. Soares P, Silva C, Chavarria D, Silva FSG, Oliveira PJ, Borges F. Drug discovery and amyotrophic lateral sclerosis: emerging challenges and therapeutic opportunities. Ageing Res Rev. 2023;83:101790.
10. Forostyak S, Sykova E. Neuroprotective potential of cell-based therapies in ALS: from bench to Bedside. Front Neurosci. 2017;11:591.
11. Magota H, Sasaki M, Kataoka-Sasaki Y, Oka S, Ukai R, Kiyose R, Onodera R, Kocsis JD, Honmou O. Repeated infusion of mesenchymal stem cells maintain the condition to inhibit deteriorated motor function, leading to an extended lifespan in the SOD1G93A rat model of amyotrophic lateral sclerosis. Mol Brain. 2021;14:76.
12. Uccelli A, Milanese M, Principato MC, Morando S, Bonifacino T, Vergani L, Giunti D, Voci A, Carminati E, Giribaldi F, et al. Intravenous mesenchymal stem cells improve survival and motor function in experimental amyotrophic lateral sclerosis. Mol Med. 2012;18:794–804.
13. Barczewska M, Grudniak M, Maksymowicz S, Siwek T, Oldak T, Jezierska-Wozniak K, Gladysz D, Maksymowicz W. Safety of intrathecal injection of Wharton's jelly-derived mesenchymal stem cells in amyotrophic lateral sclerosis therapy. Neural Regen Res. 2019;14:313–8.
14. Petrou P, Kassis I, Levin N, Paul F, Backner Y, Benoliel T, Oertel FC, Scheel M, Hallimi M, Yaghmour N, et al. Beneficial effects of autologous mesenchymal stem cell transplantation in active progressive multiple sclerosis. Brain. 2020;143:3574–88.
15. Sykova E, Cizkova D, Kubinova S. Mesenchymal stem cells in treatment of spinal cord Injury and Amyotrophic lateral sclerosis. Front Cell Dev Biol. 2021;9:695900.
16. Sun YQ, Zhang YL, Li X, Deng MX, Gao WX, Yao Y, Chiu SM, Liang XT, Gao F, Chan CW, et al. Insensitivity of human iPS cells-derived mesenchymal stem cells to Interferon-γ-induced HLA expression potentiates repair efficiency of Hind limb ischemia in Immune Humanized NOD Scid Gamma mice. Stem Cells. 2015;33:3452–67.
17. Gao WX, Sun YQ, Shi JB, Li CL, Fang SB, Wang D, Deng XQ, Wen WP, Fu QL. Effects of mesenchymal stem cells from human induced pluripotent stem cells on differentiation, maturation, and function of dendritic cells. Stem Cell Res Ther 2017, 8.
18. Abati E, Bresolin N, Comi G, Corti S. Advances, challenges, and perspectives in translational stem cell therapy for amyotrophic lateral sclerosis. Mol Neurobiol. 2019;56:6703–15.
19. Colombo M, Raposo G, Thery C. Biogenesis, secretion, and intercellular interactions of exosomes and other extracellular vesicles. Annu Rev Cell Dev Biol. 2014;30:255–89.
20. Vatsa P, Negi R, Ansari UA, Khanna VK, Pant AB. Insights of Extracellular vesicles of mesenchymal stem cells: a prospective cell-free Regenerative Medicine for neurodegenerative disorders. Mol Neurobiol. 2022;59:459–74.
21. Zhang ZG, Buller B, Chopp M. Exosomes - beyond stem cells for restorative therapy in stroke and neurological injury. Nat Rev Neurol. 2019;15:193–203.
22. Herman S, Fishel I, Offen D. Intranasal delivery of mesenchymal stem cells-derived extracellular vesicles for the treatment of neurological diseases. Stem Cells. 2021;39:1589–600.
23. Perets N, Betzer O, Shapira R, Brenstein S, Angel A, Sadan T, Ashery U, Popovtzer R, Offen D. Golden exosomes selectively target brain pathologies in neurodegenerative and neurodevelopmental disorders. Nano Lett. 2019;19:3422–31.
24. Zhou X, Deng X, Liu M, He M, Long W, Xu Z, Zhang K, Liu T, So KF, Fu QL, Zhou L. Intranasal delivery of BDNF-loaded small extracellular vesicles for cerebral ischemia therapy. J Control Release. 2023;357:1–19.
25. Gurney ME, Pu H, Chiu AY, Dal Canto MC, Polchow CY, Alexander DD, Caliendo J, Hentati A, Kwon YW, Deng HX, et al. Motor neuron degeneration in mice that express a human Cu,Zn superoxide dismutase mutation. Science. 1994;264:1772–5.
26. Fang SB, Zhang HY, Wang C, He BX, Liu XQ, Meng XC, Peng YQ, Xu ZB, Fan XL, Wu ZJ, et al. Small extracellular vesicles derived from human mesenchymal stromal cells prevent group 2 innate lymphoid cell-dominant allergic airway inflammation through delivery of miR-146a-5p. J Extracell Vesicles. 2020;9:1723260.
27. Maza AM, Jarvis S, Lee WC, Cunningham TJ, Schiavo G, Secrier M, Fratta P, Sleigh JN, Fisher EMC, Sudre CH. NMJ-Analyser identifies subtle early changes in mouse models of neuromuscular disease. Sci Rep 2021, 11.
28. Wu D, Chen Q, Chen XJ, Han F, Chen Z, Wang Y. The blood-brain barrier: structure, regulation, and drug delivery. Signal Transduct Target Therapy 2023, 8.
29. Sironi F, De Marchi F, Mazzini L, Bendotti C. Cell therapy in ALS: an update on preclinical and clinical studies. Brain Res Bull. 2023;194:64–81.
30. Moon GJ, Sung JH, Kim DH, Kim EH, Cho YH, Son JP, Cha JM, Bang OY. Application of mesenchymal stem cell-derived extracellular vesicles for stroke: Biodistribution and MicroRNA Study. Translational Stroke Res. 2019;10:509–21.
31. Shimizu M, Shiraishi N, Tada S, Sasaki T, Beck G, Nagano S, Kinoshita M, Sumi H, Sugimoto T, Ishida Y et al. RGMa collapses the neuronal actin barrier against disease-implicated protein and exacerbates ALS. Sci Adv 2023, 9.
32. Guichard JL, Kane MS, Grenett M, Sandel M, Benavides GA, Bradley WE, Powell PC, Darley-Usmar V, Ballinger SW, Dell'Italia LJ. Mitochondrial haplotype modulates genome expression and mitochondrial structure/function in cardiomyocytes following volume overload. Am J Physiol Heart Circ Physiol. 2023;324:H484–93.
33. Neikirk K, Lopez EG, Marshall AG, Alghanem A, Krystofiak E, Kula B, Smith N, Shao JQ, Katti P. Hinton AJr: call to action to properly utilize electron microscopy to measure organelles to monitor disease. Eur J Cell Biol 2023, 102.
34. Irvin CW, Kim RB, Mitchell CS. Seeking homeostasis: temporal trends in respiration, oxidation, and calcium in SOD1 G93A amyotrophic lateral sclerosis mice. Front Cell Neurosci 2015, 9.
35. Jeyachandran A, Mertens B, McKissick EA, Mitchell CS. Type I Vs. type II cytokine levels as a function of SOD1 G93A mouse amyotrophic lateral sclerosis Disease Progression. Front Cell Neurosci 2015, 9.
36. van Erp IAM, Michailidou I, van Essen TA, van der Jagt M, Moojen W, Peul WC, Baas F, Fluiter K. Tackling Neuroinflammation after Traumatic Brain Injury: complement inhibition as a therapy for secondary Injury. Neurotherapeutics. 2023;20:284–303.
37. Berkowitz S, Chapman J, Dori A, Gofrit SG, Maggio N, Shavit-Stein E. Complement and Coagulation System Crosstalk in synaptic and neural conduction in the Central and Peripheral Nervous systems. Biomedicines 2021, 9.
38. Alawieh A, Langley EF, Weber S, Adkins D, Tomlinson S. Identifying the role of complement in triggering Neuroinflammation after Traumatic Brain Injury. J Neurosci. 2018;38:2519–32.
39. Mercurio D, Oggioni M, Fumagalli S, Lynch NJ, Roscher S, Minuta D, Perego C, Ippati S, Wallis R, Schwaeble WJ, De Simoni MG. Targeted deletions of complement lectin pathway genes improve outcome in traumatic brain injury, with MASP-2 playing a major role. Acta Neuropathol Commun. 2020;8:174.
40. Sivandzade F, Prasad S, Bhalerao A, Cucullo L. NRF2 and NF-κB interplay in cerebrovascular and neurodegenerative disorders: molecular mechanisms and possible therapeutic approaches. Redox Biol 2019, 21.

41. Lee JD, Levin SC, Willis EF, Li R, Woodruff TM, Noakes PG. Complement components are upregulated and correlate with disease progression in the TDP-43(Q331K) mouse model of amyotrophic lateral sclerosis. J Neuroinflammation. 2018;15:171.
42. Shavit-Stein E, Abu Rahal I, Bushi D, Gera O, Sharon R, Gofrit SG, Pollak L, Mindel K, Maggio N, Kloog Y et al. Brain protease activated receptor 1 pathway: a therapeutic target in the Superoxide dismutase 1 (SOD1) mouse model of amyotrophic lateral sclerosis. Int J Mol Sci 2020, 21.
43. Rheaume BA, Xing J, Lukomska A, Theune WC, Damania A, Sjogren G, Trakhtenberg EF. Pten inhibition dedifferentiates long-distance axon-regenerating intrinsically photosensitive retinal ganglion cells and upregulates mitochondria-associated Dynlt1a and Lars2. *Development* 2023, 150.
44. Babaev O, Cruces-Solis H, Chatain CP, Hammer M, Wenger S, Ali H, Karalis N, de Hoz L, Schlüter OM, Yanagawa Y et al. IgSF9b regulates anxiety behaviors through effects on centromedial amygdala inhibitory synapses. Nat Commun 2018, 9.
45. Woo J, Kwon SK, Nam J, Choi S, Takahashi H, Krueger D, Park J, Lee Y, Bae JY, Lee D, et al. The adhesion protein IgSF9b is coupled to neuroligin 2 via S-SCAM to promote inhibitory synapse development. J Cell Biol. 2013;201:929–44.
46. Martínez-García A, Sastre I, Recuero M, Aldudo J, Vilella E, Mateo I, Sánchez-Juan P, Vargas T, Carro E, Bermejo-Pareja F, et al. :, a gene involved in oxidative stress Induced Death, is Associated with Alzheimer's Disease. J Alzheimers Disease. 2010;22:1181–7.
47. Gan YL, Wang CY, He RH, Hsu PC, Yeh HH, Hsieh TH, Lin HC, Cheng MY, Jeng CJ, Huang MC, Lee YH. FKBP51 mediates resilience to inflammation-induced anxiety through regulation of glutamic acid decarboxylase 65 expression in mouse hippocampus. J Neuroinflamm 2022, 19.
48. Giunti D, Marini C, Parodi B, Usai C, Milanese M, Bonanno G, Kerlero de Rosbo N, Uccelli A. Role of miRNAs shuttled by mesenchymal stem cell-derived small extracellular vesicles in modulating neuroinflammation. Sci Rep. 2021;11:1740.

## Publisher's Note